

Intrinsic Negative Magnetoresistance in Layered AFM Semimetals: the Case of EuSn_2As_2

K. S. Pervakov,¹ A.V. Sadakov,¹ O. A. Sobolevskiy,¹ V. A. Vlasenko,¹ V. P. Martovitsky,¹
E. A. Sedov,^{1,2} E. I. Maltsev,^{3,4} N. Pérez,^{3,4} L. Veyrat,^{3,4,5} P. D. Grigoriev,⁶ N. S.
Pavlov,^{7,1} I. A. Nekrasov,⁷ O. E. Tereshchenko,⁸ V. A. Golyashov,⁸ and V. M. Pudalov^{1,2}

¹*V. L. Ginzburg Research Center at P. N. Lebedev Physical Institute, RAS, Moscow 119991, Russia.*

²*HSE University, Moscow 101000, Russia*

³*Leibniz Institute for Solid State and Materials Research, IFW, 01069 Dresden, Germany*

⁴*Dresden-Würzburg Cluster of Excellence ct.qmat, Dresden, Germany*

⁵*Laboratoire National des Champs Magnétiques Intenses,
CNRS-INSA-UJF-UPS, F-31400 Toulouse, France*

⁶*L.D. Landau Institute of Theoretical Physics, RAS*

⁷*Institute for Electrophysics, RAS, Ekaterinburg, 620016, Russia*

⁸*Institute for Semiconductor Physics, RAS, Novosibirsk, Russia*

Here, by applying a comprehensive approach including magnetic, transport measurements, ARPES band structure measurements, DFT calculations, and analytical theory consideration, we unveil the puzzling origin of the negative isotropic magnetoresistance in the highly anisotropic semimetals, particularly, $\text{Eu}_2\text{Sn}_2\text{As}_2$ with AFM ordering of Eu atoms. The isotropic magnetoresistance developing along with the magnetization changes up to the complete spin polarization field was reported previously in several experimental studies, though its theoretical explanation was missing up to date. Recently, we proposed a novel theoretical mechanism to describe the observed magnetoresistance in layered AFM compounds by exchange splitting of the electron energy levels and by confining the electron wave functions with different spin projection in the vicinity of the respective magnetic layer. In this paper, we present more detailed experimental studies of the negative magnetoresistance with several samples of EuSn_2As_2 in order to identify its sample-independent features including temperature dependence. We also substantiate the proposed theory by comparing it with magnetotransport data, with ARPES measurements of the energy band structure, and DFT energy spectrum calculations.

I. INTRODUCTION

The van der Waals materials with magnetically ordered atomic layers have inspired great scientific interests in different fields due to their tunable ground states [1–4]. These layered materials are attracting from fundamental point of view because can host interesting topological states, such as quantum anomalous Hall state, chiral anomaly, Chern insulator, higher-order topological Möbius insulator, etc. Among them, of a special interest are intrinsic (stoichiometric) materials with significant spin-orbit and exchange coupling, since disorder effects can be suppressed to a large extent, which is expected to facilitate the virgin quantum phenomena.

These compounds host sublattice of large spin atoms (Eu, Mn, Co, etc), which order antiferromagnetically upon lowering temperature, and layers of Se, As, Te supplying electrons at the Fermi level. The most famous and most studied compound is MnBi_2Te_4 an intrinsic topological insulator (TI) with antiferromagnetic (AFM) ordering of Mn-ions, that manifests fascinating physics. Less explored (though not less interesting) are topologically trivial stoichiometric Eu-based semimetals, such as EuSn_2As_2 [5–11], EuSn_2P_2 [14, 15], EuFe_2As_2 [4, 16–18], and Co-based semimetals - CaCo_2As_2 [19], and CsCo_2Se_2 [20]. These “122-compounds” are also building blocks of more complex remarkable materials, such as e.g. $\text{EuRbFe}_4\text{As}_4$ [21, 22], the high- T_c -superconductor

with AFM ordering of Eu atoms.

All the layered non-Weyl AFM semimetals exhibit a negative magnetoresistance (NMR). The most puzzling is the fact that the magnetoresistance in the highly anisotropic layered compounds is fully isotropic. Despite the fact that this isotropic negative magnetoresistance (NIMR) is well documented experimentally, its theoretical interpretation was missing, until recently. In topologically trivial semimetals (EuSn_2As_2 , EuSn_2P_2 , CaCo_2As_2 , and CsCo_2Se_2) NIMR is approximately similar: it has a magnitude about 3-6%, nearly parabolic shape $\delta R(H)/R(0) \propto -\alpha H^2$, and is isotropic with respect to the field direction and current direction [10, 11, 19]. As field increases, this parabolic negative magnetoresistance sharply terminates, exactly at the field of complete spin polarization H_{sf} , and further changes to a conventional positive magnetoresistance. Thus, the NMR correlates closely with the magnetization $M(H)$ characteristics [6, 10, 11]. Earlier, the negative magnetoresistance in layered AFM semimetals was suggested to associate with either nontrivial topological properties, or with scattering by magnons, domains, magnetic impurities. We showed in Ref. [23] and explain in more detail in this paper that none of the previously known mechanisms is capable to explain the observed negative isotropic magnetoresistance.

In view of the remarkable magnetoresistance isotropy, we introduced in Ref. [23] a novel mechanism of NIMR

that implies only point-like scattering of electrons and provides the isotropy of the NIMR. Within the framework of this mechanism, the driving force of the NIMR is the exchange splitting of the energy bands in the AFM polarized sublattices. It modifies spatial distribution of the wave function of spin-up and spin-down electrons and leads to the magnetization-dependent enhancement of scattering rate. Though the close relationship between magnetization and magnetoresistance is well known also for giant magnetoresistance (GMR) in layered Fe/Cr superlattices and for colossal magnetoresistance (CMR) in granular samples and in manganites [24–27], the novel mechanism [23] is completely different and provides isotropic negative magnetoresistance.

In the current paper we provide more details of the proposed theory of NIMR [23], present extended experimental data on transport, magnetotransport, magnetization and band structure of EuSn_2As_2 single crystals. Firstly, we show that the observed NIMR is an *intrinsic* (i.e. irrelevant to structural defects) property of the layered AFM materials with strong spin-orbit and exchange splitting. This conclusion is based on transport measurements with samples of various thicknesses (from 140nm to 500nm), magnetization and ARPES measurements, DMFT band structure calculations, and high precision XRD and TEM examination of the crystal perfection.

Secondly, we test the novel theoretical mechanism and show that it qualitatively explains the observed NIMR. In the proposed mechanism, NIMR originates from the enhancement of the usual short-range scattering of conducting electrons by the alternating sublattice magnetization in the layered AFM crystal. Therefore, this NIMR mechanism may be applicable not only to EuSn_2As_2 , but also to a wide class of the layered AFM semimetals, independent of their topology.

The paper is organized as follows. In Section II we describe crystal lattice, samples and their characterization. In section III we present our results of band structure ARPES measurements and DMFT calculations, in section IV we present the main experimental data of magnetization, and in section V - of magnetotransport measurements, particularly, we show full isotropy of the NIMR with respect to the field direction and current direction. In section VI we introduce the basic idea of the model. In section VII we compare our calculations with experimental data. Finally, we provide a brief summary and discussion of the results in section VIII. In Appendices I, II and III we analyse difference in the NMR shape for various samples, discuss the relevance of various scattering mechanisms to NIMR, and present a detailed theoretical derivation of NIMR. Supplemental materials [28] contain additional information on the crystal synthesis, XRD examination of the lattice structure, energy spectrum measurements (ARPES) and calculations.

Although our experimental studies are performed with EuSn_2As_2 , the magnetoresistance effect we explore is common for a number of the above listed layered compounds.

II. LATTICE STRUCTURE. SAMPLES AND THEIR CHARACTERIZATION

In EuSn_2As_2 , at $T < 24\text{K}$ the magnetic Eu-sublattice orders in the A-type AFM structure (AFMa) in which Eu magnetic moments lie in the ab -plane and rotate by π from layer to layer (Fig. 1). By combining first principles calculations and time-resolved tr-ARPES measurements, Li et al. [9] suggested that EuSn_2As_2 is an intrinsic AFM topological insulator. Our low temperature magnetotransport as well as ARPES studies and DFT calculations (Sec. III) however, show that EuSn_2As_2 is the non-Weyl semimetal, rather than TI.

The layered EuSn_2As_2 compound has a space group $R\bar{3}m$, where each trigonal Eu layer is sandwiched between two buckled honeycomb SnAs layers (Fig. 1), located at a distance $c_0 \approx 2.4\text{\AA}$ apart [8]. The overall height of the elementary cell is $c \approx 26.4\text{\AA}$ (for more detail, see SM [28]). The charge carriers are supplied to the band from SnAs layers confined between the layers of Eu (see Section III, and SM [28]). At low temperatures, below the Neel temperature $T_N \approx 22 - 24\text{K}$, the carriers experience the static alternating magnetization of ferromagnetically ordered individual Eu layers.

Transport measurements were done with bulk crystals, approximately (1 – 2.5) mm in the ab -plane and (0.1 – 0.5) mm thick (Fig. 2, inset), and with exfoliated thin flakes (Fig. 1b,c). Two bulk samples have been studied most intensively: sample #1-1 with a thickness of 0.5 mm after growth already had one flat mirror surface and was not cleaved. Sample #2 was cleaved down to thickness of 0.1 mm and shaped rectangular. Au/Ti contact pads were deposited through a contact mask on the face and bottom sides of the bulk samples. 30- μm Au-wires were attached to the contact pads using conducting silver paint.

We also studied the flake exfoliated from the bulk crystal with lateral dimensions $\sim 5 \times 10\mu\text{m}$ in the ab -plane and thickness 140 nm in the c direction (Fig. 1c). Further studies on the flakes are presented elsewhere [Ref. [29]]. Electrical leads and contact pads to the flake were made of Au/Ti film evaporated by e-beam gun and patterned using laser lithography. Underneath the contacts the flake was thinned down to 40 nm in order to provide more stable Au/Ti contacts.

The resistance components were measured using four probe AC-technique: the diagonal R_{xx} component was measured with bulk crystals and flakes, whereas Hall resistance R_{xy} was measured only with flakes, using lithographically defined four or more contacts. Two setups were used for bulk samples. For measuring in-plane resistance, R_{ab} , the bias current was applied through the contacts at one ab -surface and voltage drop was measured between two potential contacts deposited at one of the ab -surfaces. For measuring R_c component, bias current was applied along c axis and voltage drop was measured between potential contacts deposited at two opposite ab -sides. An example of contacts configuration for flakes is shown in Fig. 1c, and for bulk sample – in the inset to

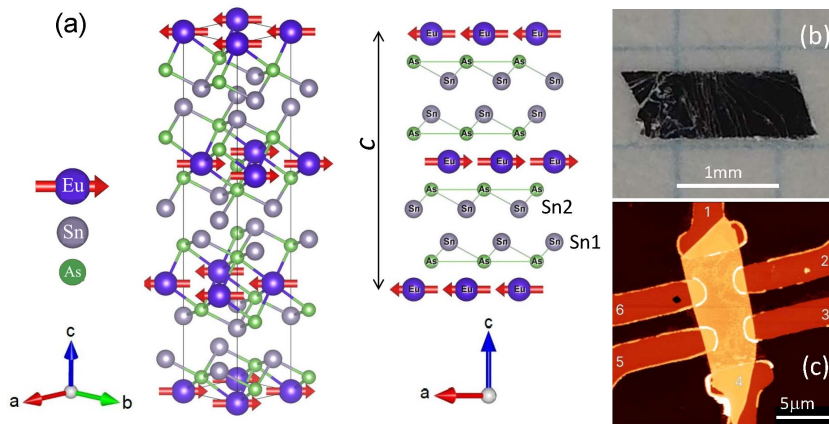


FIG. 1. (a) Lattice structure of the EuSn_2As_2 , 3D-view and 2D projection on the $a-c$ plane. Magenta arrows show Eu-atoms magnetization direction in the A-type AFM ordered state. (b) Typical bulk crystal. (c) Top view of the 140-nm-thick exfoliated flake with Au contact stripes [29]. Horizontal white bar shows $5\ \mu\text{m}$ scale.

Fig. 2. Two resistance components R_{xx} and R_{xy} were measured in different magnetic sweeps due to limitation of the setup.

Temperature dependences of the diagonal resistance components, in-plane R_{ab} , and normal to the plane, R_c , in zero field are shown in Fig. 2. Both components R_{ab} and R_c show a kink, 1-2% high, at temperature of the AFM ordering $T_N \approx 24\text{K}$. The increase in resistivity near T_N is likely due to scattering of delocalized conduction electrons by the fluctuating localized Eu^{2+} magnetic moments beginning to order in the vicinity of T_N [30]. Such behavior in the vicinity of magnetic ordering temperature was previously observed for EuSn_2As_2 [5, 6, 10], for EuSn_2P_2 [15] and for EuIn_2As_2 [31].

Both ρ_{ab} and ρ_c components exhibit a typical semimetallic temperature dependence consistent with that reported earlier [5, 6, 10, 11]. The resistance gradually decreases with lowering temperature from 300K to 30K by a factor of ≈ 1.4 for the bulk and for the 140nm-thick flake, displaying no contribution from the predicted bulk insulator and Dirac surface states [9]. Below the kink, both resistivity components continue decreasing down to our lowest $T = 2\text{K}$, with a difference that R_{ab} decreases steeper than R_c . This is consistent with the gapless band structure revealed in our ARPES measurements and band structure calculations (Section III), and also consistent with previous studies in Ref. [9]. The interlayer resistivity ρ_c was measured only with bulk crystal; it is a factor of 130 larger than the in-plane component, whereas the temperature dependences of both components are similar when scaled down by the anisotropy factor. The huge resistivity anisotropy $\rho_c/\rho_{ab} \sim 130$ is qualitatively consistent with highly anisotropic crystal structure, where $c \approx 26.4\text{\AA}$, $a, b \approx 4.22\text{\AA}$ (see Fig. 1, SM [28], and also Ref. [5]).

Our data for all studied samples doesn't confirm a superconducting transition below 4.8K contrary to that reported in Ref. [32]. In measurements with bulk crys-

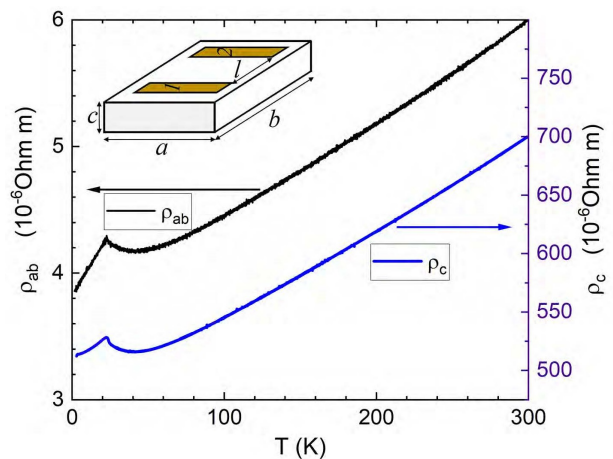


FIG. 2. Temperature dependences of the resistivity components at zero field for bulk sample #2: in-plane ρ_{ab} , and normal to the basal plane ρ_c . Insert shows schematics of the sample and contact arrangement. $a = 1.1\text{mm}$, $b = 2.6\text{mm}$, $c \approx 0.1 \pm 0.03\text{mm}$, $l = 2\text{mm}$. 1, 2 - current contact pads, and 3, 4 (underneath, invisible) - potential contacts.

tals and flakes we didn't observe also a nonmonotonic $\rho(H)$ and $M(H)$ behavior at $H > 5\text{T}$ as that reported in Ref. [11].

III. BAND STRUCTURE ARPES MEASUREMENTS AND DFT CALCULATIONS

Band structure of the crystal surface was investigated by angle resolved photoemission spectroscopy (ARPES). Measurements were done using He-I α radiation ($h\nu = 21.22\text{eV}$) of a nonmonochromated He-discharge lamp (UVS-300, SPECS GMBH) and an hemispherical electron energy analyzer equipped with electrostatic deflector (ASTRAIOS-190, SPECS GMBH). The samples were

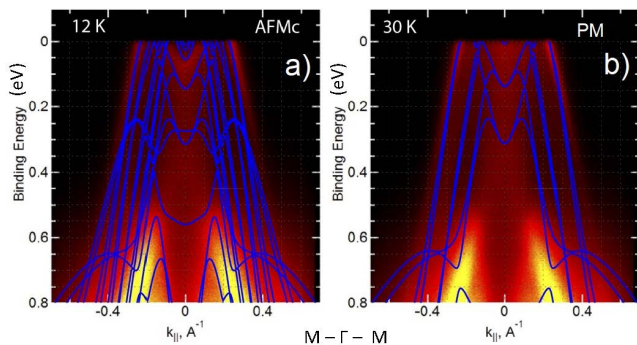


FIG. 3. Electronic structure of EuSn_2As_2 bulk crystal below E_F along $M-\Gamma-M$ direction. (a) in the AFM state at $T = 12\text{K}$, and (b) in the PM state at $T = 30\text{K}$. Color intensity map - ARPES measurements at photon energy $h\nu = 21.2\text{eV}$. Blue lines show the calculated dispersion in the AFM and PM state.

cleaved in situ in a vacuum of 5×10^{-10} mbar at room temperature. Low energy electron diffraction (LEED) measurements showed clear 1×1 diffraction patterns and confirmed the cleaved crystal (0001) surfaces to be free from any reconstruction. The results are presented in Fig. 3 for the $M-\Gamma-M$ direction for low binding energies 0 - 0.8eV.

Data for a wider energy range and for the $k_x - k_y$ cut at the Fermi level is given in SM [28]. When our ARPES data are considered in the wide energy range from 0 to -4.5eV [28], the overall energy spectrum is very similar to that measured earlier [9], calculated in Ref. [8], and also shown in Fig. 4. We focus here on the low-energy region in the vicinity of the Fermi level, since namely these quasiparticles participate in the multi-band semimetallic transport at low temperatures. In the vicinity of the Γ point there is an electron-like pocket, surrounded by several enclosed hole bands (which presumably have a corrugate cylinder shape). Other electron bands theoretically predicted to be around M point, and a surface topological states at Γ point are not seen at $E \leq E_F$, in agreement with Ref. [9]. Both the hole- and electron levels in the AFM state are significantly broadened, the feature that has not been discussed earlier. In Figure 3, at the $\Gamma-M$ cross-section, one can clearly see that broadening of the hole and electron pocket contours persists down to low temperatures.

The DFT band structure calculations were performed within the DFT+U approximation in the VASP software package [33]. The generalized gradient approximation (GGA) in the form of the Perdew-Burke-Ernzerhof (PBE) exchange-correlation functional [34] was employed. The onsite Coulomb interaction of Eu-4*f* electrons was described with the DFT+U scheme with the Dudarev approach [35] ($U=5.0\text{eV}$ same as in Ref. [9]). A non-collinear magnetic DFT calculations were performed with spin-orbit coupling. The calculated electron energy dispersion in AFM magnetic state is shown in Figs. 3 by the blue lines. The main contribution to the bands near

the Fermi level comes from the Sn-*p* and As-*p* orbitals.

The most important result of these calculations for clarifying the origin of NIMR (and, particularly, for substantiating our theory of NIMR [23]) is the band splitting around the Fermi level shown in more detail in Fig. 4. In a noncollinear calculation, the spin components are not easily distinguished. For distinguishing the up and down spin components, we performed calculation in the collinear spin configuration that corresponds to the AFM-*c* order.

The elementary cell of EuSn_2As_2 contains a pair of neighboring layers of Sn atoms (we call them Sn1 and Sn2 - see Fig. 1a), sandwiched between Eu layers with opposite spin projection (\uparrow and \downarrow , or “left” and “right” in Fig. 1a). The ferromagnetic magnetization of the nearest Eu-neighbor leads to magnetization of the Sn-5*p* state and to the spatial separation of the oppositely magnetized \downarrow, \uparrow Sn-5*p* states [23]. Contribution of As-4*p* states to the bands at the Fermi level is not large, therefore we consider only Sn-5*p* orbital resolved bands.

Some of the energy levels for Sn-5*p* states with \downarrow, \uparrow spin coincide with each other (see Fig. 4). However, near the Γ -point and slightly below the Fermi level, the Sn-5*p* bands with \downarrow, \uparrow spin projection are split in energy by about 30-40 meV. The splitting is well seen above the Fermi level and the given above value corresponds to the Sn-5*p* state. The presence of bands splitting indicates that these states are affected by exchange interaction. Moreover, the Sn1 contribution with spin up is almost the same as Sn2 with spin down. As a result, the Sn1 and Sn2 layers are predominantly magnetized in opposite directions depending on which Eu atom is closer. This spatial separation of the oppositely magnetized Sn layers is confirmed by our DFT calculations in Ref. [23].

In order to illustrate that the level splitting originates mostly from exchange, we compare in Fig. 4e the calculated band structure in the AFM-*c* and paramagnetic (PM) states. One can see in the same region near the Γ -point and slightly below Fermi level (see the insert to Fig. 4e) that the PM bands (blue lines) almost coincide at $k \sim 0.05\text{\AA}^{-1}$. There are several PM bands due to the presence of 6 such pairs of Sn layers in the unit cell. In contrast, in the AFM state, the bands at the same region are split. The splitting may be due to hopping along z axis (crystallographic *c*-direction) between layers and due to exchange interaction. Since the bands in this region collapse in the paramagnetic solution, it suggests that the splitting has the exchange nature. In the earlier investigation Ref. [36], the band splitting was also found in calculation without spin-orbit coupling for AFM solution (see the SST4 case [36]).

The agreement of our calculations with Ref. [36] supports the exchange origin of the bands splitting in the AFM state. The value of exchange interaction is estimated namely from splitting in this region, because the bands with opposite spin always coincide in the conventional AFM state. Therefore, the splitting of Sn-bands with opposite spin is a “smoking gun evidence” for the

exchange interaction origin of the splitting.

To summarize this section: Figure 4e clearly shows that in the PM state (blue lines) the Sn- bands almost coincide, and a minor difference between them is due to the presence of 6 such pairs of Sn layers in the elementary cell. In the AFM state, the bands with opposite spins for one Sn atom are essentially split (see Fig. 4e and the inset). We also note, that earlier in Ref. [36] the band splitting without spin-orbit contribution was also found in the AFM state (SST4 case), which supports our result.

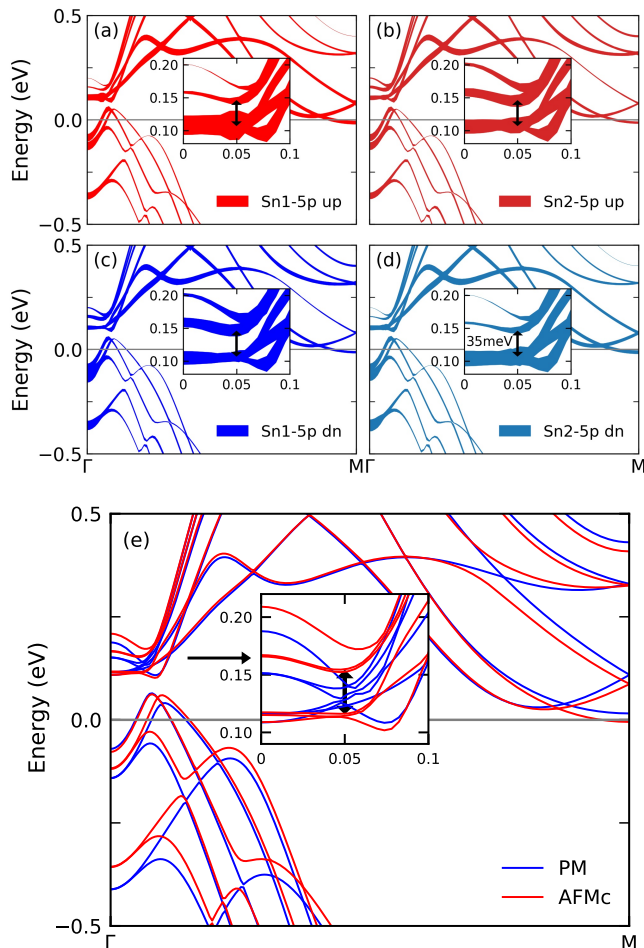


FIG. 4. Band structure of EuSn_2As_2 with orbital and spin contributions for Sn-5p states from the 1st layer Sn1 (see panels a,c) and from the 2nd layer Sn2 (panels b,d). The band width corresponds to orbital contribution to the band. (e) Comparison of the band structure in AFMc (red lines) and PM (blue lines) state with the same double-size along c axes unit cell. The insert shows an enlarged region of splitting. Vertical arrows show the exchange splitting.

IV. MAGNETIZATION MEASUREMENTS

Magnetization measurements were done using MPMS-7 SQUID magnetometer, with bulk samples, solely. Fig-

ure 5 shows evolution of the DC-magnetization curves $M(H_{ab}, T)$ and $M(H_s, T)$, measured for field orientations, in-plane $H \parallel ab$ and perpendicular to the plane $H \perp ab$ (or, equivalently, $H \parallel c$), respectively, at various temperatures, from the antiferromagnetic state $T < T_N$ to paramagnetic state $T > T_N$. The $M(H, T)$ curves follow the conventional field dependence for the A-type easy-plane antiferromagnet [37, 38], fully consistent with our previous measurements on similar samples [7, 23], and also similar to those reported in other works for EuSn_2As_2 [5, 6, 9, 10]. The magnetization saturation corresponds to the full spin polarization; for our lowest temperatures this occurs at $H_s \approx 4.7\text{T}$ when H is parallel to the c -axis, and at $H_s \approx 3.4\text{T}$ when H lies in the easy magnetization ab -plane. Extrapolated to $T = 0$ the spin polarization fields equal $H_s(0) = 4.8$ and 3.5T , respectively

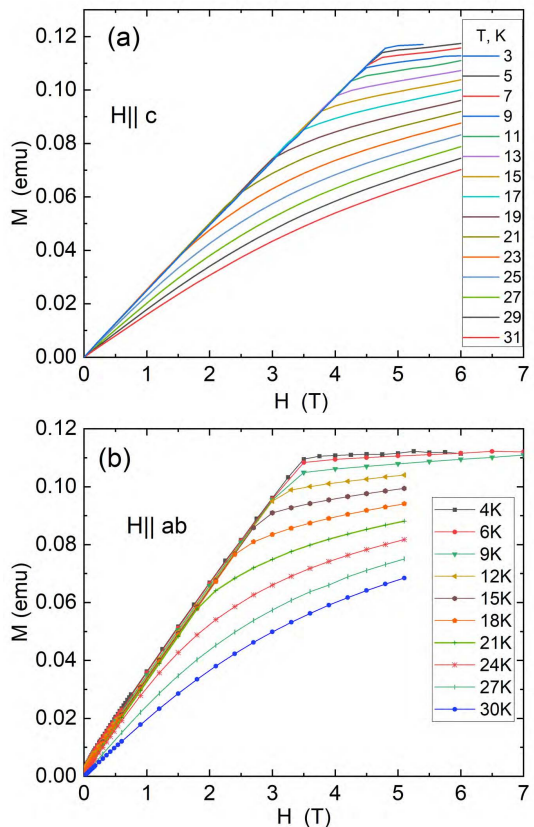


FIG. 5. (a,b) DC-magnetization $M(H)$ for bulk crystal #2 (with a mass of 1.8 mg) at various temperatures for two field orientations. Temperature values are indicated on the panels.

When field is perpendicular to the ab -plane, the magnetization curves $M(H \parallel c)$ at the lowest temperatures are precisely linear in the field range from zero and up to H_s (Fig. 5a). In the field interval of 5-10 T we didn't observe a two-stage $M(H)$ saturation as that reported in [11] above $\approx 4\text{T}$. For field in the ab plane, there is a weak nonlinearity of $M(H)$ in low fields less than $\approx 0.03\text{T}$, visible at the lowest temperatures in Fig. 5b. Similar non-

linearity of $M(H)$ may be noticed also in the preceding papers [6, 9–11]. We investigated the $M(H)$ nonlinearity and the $\chi(T)$ divergence in detail in Ref. [39] and have shown that these effects are caused by planar defects in the crystal lattice which behave below $T \approx 24\text{K}$ as weak ferromagnets embedded into the AFM matrix.

V. MAGNETOTRANSPORT RESULTS

Magnetotransport data were collected with PPMS-16 and CFMS-16 measuring systems in fields up to 16 T, using 4-probe measuring set-up.

A. Hall resistance measurements

Hall voltage was measured only for the flakes, in fields directed perpendicular to the ab -plane. For Hall voltage measurements, we used one of the two pairs of lithographically defined potential probes (see Fig. 1c). The results shown in Fig. 6 demonstrate that the Hall resistance and, hence, carrier density, almost don't vary with temperature in the range from 2.8 to 15 K. The absence of T -dependence of the Hall effect is in line with the diffusive (“metallic”) transport character and signals the negligible contribution of the topological surface states (if any).

In fields $H \sim \pm 5\text{T}$, the Hall resistance $R_{xy}(H)$ changes slope. In higher fields $R_{xy}(H)$ tends to become linear, and from its slope, $dR_{xy}/dH \approx 4.4 \times 10^{-2}\text{Ohm/T}$, assuming the single band model one could roughly estimate the density value $n \approx 10.15 \times 10^{26}/\text{m}^3$ (using the measured flake thickness $d = 140\text{nm}$). This density value is by a factor of 2 higher than that reported in Refs. [6, 10, 11]. However, as we show below, this estimate has little to do with reality, since the energy spectrum in the vicinity of E_F (see Figs. 3, 4, and also Fig. 20 of SM) consists of several bands (holes and electrons), whose contributions to R_{xy} significantly compensate each other. For simplicity, we consider only the two band case, where the charge transport is determined by four parameters: n_h, n_e and μ_h, μ_e - the hole and electron densities and mobilities, respectively.

In order to solve the four parameter problem, we turn to the non-linear field dependence of the Hall voltage shown in Fig. 6. The nonlinear $R_{xy}(H)$ dependence was noticed earlier and was attributed to the anomalous Hall effect in Refs. [11, 40]. We argue that for EuSn_2As_2 the $R_{xy}(H)$ non-linearity, in the lowest approximation, is a simple consequence of the two-band charge transport.

Indeed, the energy spectrum (Figs. 3 and 4) clearly shows the presence of the two major bands at the Fermi level - the larger hole and the smaller electron pockets. Within the two-band concept, and considering, for simplicity, only the in-plane current direction $\mathbf{j} \parallel (ab)$, i.e. ignoring the case of $\mathbf{j} \parallel c$, we arrive at the 2D geometry of

TABLE I. Numerical parameters obtained from fitting experimental data with the two-band model. $n_{e,h}$ is in units of $[10^{20}/\text{cm}^3]$, $\mu_{e,h}$ in $[\text{cm}^2/\text{Vs}]$.

n_h	n_e	μ_h	μ_e	Data fitting:
0.99	0.286	134	230	Hall: $R_{ab}(H \parallel c)$, flake 140nm

measurements. Thus, for $H \perp (ab)$, $\mathbf{j} \in (ab)$ in the moderate field range $\omega_c\tau \equiv \mu H \leq 1$, by neglecting terms of the order $(\omega_c\tau)^4$, neglecting electron-electron interaction corrections [41], and assuming isotropic scattering, the conductivity tensor may be written as

$$\sigma_{jk} = \sum_{i=1}^2 \frac{e_i n_i \mu_i}{1 + (\mu_i H)^2} \begin{pmatrix} 1 & \pm \mu_i H \\ \mp \mu_i H & 1 \end{pmatrix}. \quad (1)$$

Here, $n_1 \equiv n_h$, $n_2 \equiv n_e$, $\mu_1 \equiv \mu_h$, $\mu_2 \equiv \mu_e$, and $e_i = \pm e$ - the elementary charge of holes and electrons, respectively. By inverting the conductivity tensor and keeping only terms up to $(\omega_c\tau)^3$ we obtain for the off-diagonal resistivity component:

$$\rho_{xy} = \frac{H}{e} \frac{(n_h \mu_h^2 - n_e \mu_e^2) + (n_h - n_e)(\mu_h \mu_e H)^2}{(n_h \mu_h + n_e \mu_e)^2 + (n_h - n_e)^2 (\mu_h \mu_e H)^2} \quad (2)$$

In Fig. 6 the blue dashed curve shows fitting of the experimental $R_{xy}(H)$ data with Eq. 2 using the set of parameters given in Table 1. As expected, the hole density is a factor of 3.5 larger than the electron density. Such relationship n_h/n_e is approximately consistent with the partial sizes of the hole and electron bands in the energy spectrum (Fig. 4). This set of parameters provides also the zero field diagonal resistivity value $\rho_{xx}^{\text{calc}} = n_h \mu_h + n_e \mu_e = 3.15 \mu\Omega\text{m}$ that may be compared with $\rho_{xx} = 3.85 \pm 1 \mu\Omega\text{m}$ measured for the bulk crystal (Fig. 2), and $3.01 \mu\Omega\text{m}$ for the flake. Taking into account a 25% uncertainty in the bulk crystal thickness, and large contact pads area on the flake surface (Fig. 1c), the agreement is satisfactory.

Given a good quantitative agreement between Eq. 2 and the Hall resistance data, we see no need to involve additional assumptions (e.g. such as “coupling between the localized magnetic ordering and the conduction electronic states” [11]) as a mechanism causing Hall resistance nonlinearity.

For the above density value, and assuming 3D spin-degenerate system, we estimate $k_F^h = 3.0 \times 10^7 \text{ cm}^{-1}$, $\lambda_F^h \approx 42\text{\AA}$, respectively. Thus, the wave function for the holes extends at a distance much larger than the spacing between two neighbouring Eu-planes, $\approx 6\text{\AA}$. The electron wavelength λ_F^e is even larger by a factor of ~ 1.5 . The large extension of the carrier wave functions is an important requisite of our model of the negative magnetoresistance [23].

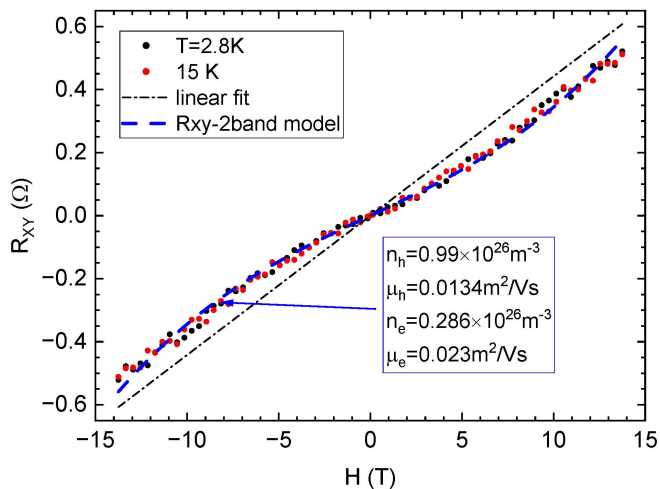


FIG. 6. Hall resistance versus perpendicular magnetic field measured with 140nm-flake: data at two temperatures, 2.8 and 15K, and the best fit with Eq. 2 (solid blue line). The fitting parameters (n_h , n_e , μ_h , μ_e) are given in Table 1. Dash-dotted line shows a single-band fitting at high fields.

B. Diagonal magnetoresistance

The overall evolution of the normal to the plane $R_c(H, T)$ and in-plane $R_{ab}(H, T)$ magnetoresistance with temperature and magnetic field is shown in Fig. 7. In view of the data complexity we discuss separately, positive and negative magnetoresistance, trivial and less-trivial magnetoresistance geometry. In all configurations, the most striking is the hump of the negative magnetoresistance (NMR) in the AFM state that is the focus of our study. In the AFM state, at $H < H_s$, as temperature increases, the NMR hump quickly gets narrower whereas its magnitude changes weaker (see Figs. 7). Close to and above T_N , it starts decreasing in magnitude, and widens in field [29]. Finally, the NMR hump gradually vanishes and transforms to the positive parabolic magnetoresistance.

1. Negative and positive magnetoresistance

Figures 7 and 8 show the $R(H)$ data for several field directions relative to the crystal axis, and for various angles between the bias current and applied field. We first describe the data on a qualitative level.

The NMR hump has several remarkable features: (i) it is similar for current applied in the ab -plane and in perpendicular direction (see Figs. 7, 9, and Appendix A), (ii) it is independent of the in-plane current direction relative to magnetic field (see Fig. 8), (iii) it amounts up to about 6% for all studied bulk samples and flakes, and (iv) it sharply terminates at the field of complete spin polarization H_s (cf. Figs. 5 and 9).

NIMR isotropy in the ab -plane. Regarding this class of

compounds, in literature an exciting axion insulator state was discussed, whose “smoking gun” evidence would be a sharp anisotropy of the magnetoresistance relative to the mutual orientation of the magnetic field and current. In order to test this possibility we measured the magnetoresistance anisotropy by rotating the sample with in-plane bias current in magnetic field aligned precisely in the ab -plane. Figure 8 shows that the magnetoresistance is fully isotropic, i.e. independent of the angle between field and current directions, thus confirming (i) EuSn₂As₂ to be topologically trivial, (ii) the magnetoresistance is irrelevant to the chiral anomaly, contrary to the suggestion in Ref. [9], and (iii) the ab plane to be the easy-magnetization plane with equivalent a and b axis.

Sample- and configuration dependent diversity of the NIMR shape. At first sight, the negative magnetoresistance looks similar for all studied samples. However, upon closer examination, we find two qualitatively different types of the functional $R(H)$ dependence: the NIMR hump is almost *parabolic* for $R_{ab}(H_{ab})$ geometry in all studied samples (Fig. 8), whereas for $R_{ab}(H_c)$ in some samples NIMR has a more *flattened* shape (Fig. 7)a,b,c. Correspondingly, we classify the results with the studied EuSn₂As₂ samples in two groups displaying either the “parabolic” or the “flattened” type $R(H)$ dependence (for more detail, see Appendix A). Below we argue that minor variations of the NIMR shape (sample-dependent, and the field-against-current orientation dependent) come partly from the contribution of classical positive MR in a two-band model with different electron and hole mobilities.

At low temperatures $T \ll T_N$, as field increases and exceeds H_s , the NIMR hump changes sharply to the smooth positive parabolic rise. We highlight that the sharp transitions between the negative and positive magnetoresistance (i.e. the $R(H)$ minima) coincide with the sharp magnetization saturation at $H = H_s$ for the respective field direction (cf. Figs. 5 and 9a). This is consistent also with previous studies [5, 10, 11, 15, 42].

2. Classical positive magnetoresistance at $H > H_s$.

Above the full spin polarization field H_s , the positive magnetoresistance (PMR) is observed in all geometries when the bias current \mathbf{j} is perpendicular to the field (Figs. 7c,d and 9a). PMR is essentially weaker when \mathbf{j} and \mathbf{H} lie in the same ab plane (see Fig. 8). These facts indicate that the positive magnetoresistance has a classical orbital character, and we further call it “classical PMR” (CPMR).

At first sight, CPMR is reminiscent of the simple textbook dependence $\delta R(H)/R(0) = (\omega_c \tau)^2 \equiv (\mu H)^2$. However, for the closed isotropic Fermi surface, within the single band transport, and neglecting electron-electron interaction corrections [41], Eq. (1) for electron-impurity scattering suggests ρ_{xx} to be strictly independent of field. In order to make a more rigorous comparison of CPMR

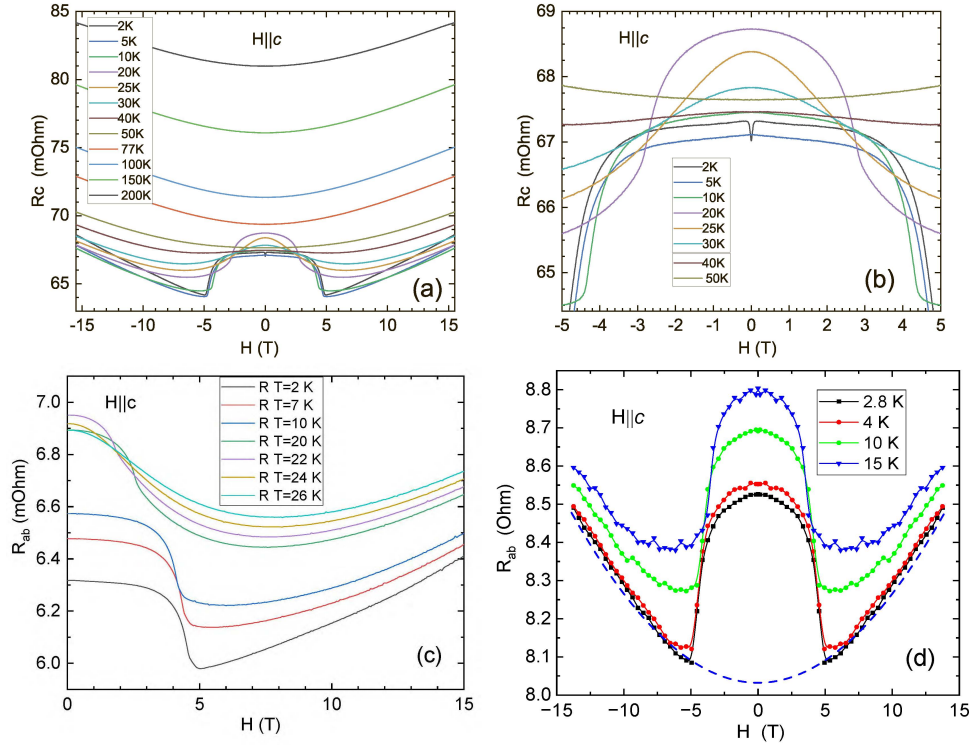


FIG. 7. (a)-(c) Examples of the “flattened”-type $R(H)$ dependences at various temperatures for $H||c$: (a) $R_c(H||c)$ for bulk crystal #2 at temperatures from 2 to 200K, and in the wide field range; (b) same, in the narrower field range for 7 temperature values; (c) $R_{ab}(H||c)$ for the bulk crystal #2 in the range 2 - 26K; (d) $R_{ab}(H||c)$ for the 140-nm thick flake at temperatures from 2.8 to 15 K. Blue dashed curve shows CPMR calculated using Eq. 3 with parameters from Table 1.

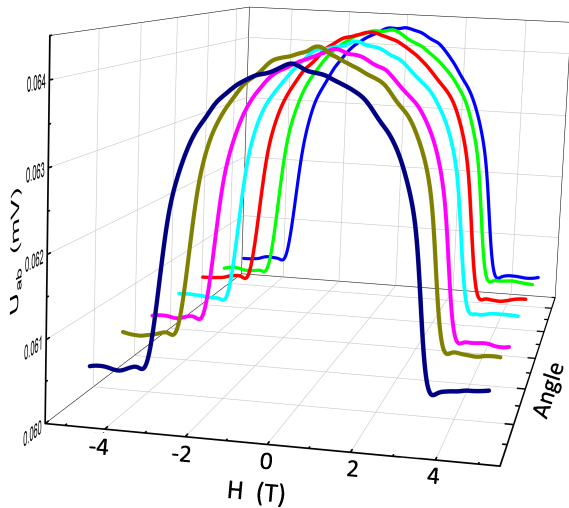


FIG. 8. Magnetoresistance in the easy-plane $R_{ab}(H||ab)$ measured for different angles (from 0 to 90°, with 15° step) between the current and field directions. z -axis - diagonal voltage drop with 100 μ A bias current.

with theory, we invert again the conductivity tensor for

the two-band system, Eq. (1), and obtain:

$$\begin{aligned} \delta\rho_{xx}(H) &= \rho_{xx}(H) - \rho_{xx}(0) \\ \rho_{xx}(0) &= \frac{1}{e(\mu_e n_e + \mu_h n_h)} \\ \rho_{xx}(H) &= \frac{1}{e} \frac{H^2(\mu_h \mu_e)(n_h \mu_e + n_e \mu_h) + n_h \mu_h + n_e \mu_e}{H^2(\mu_h \mu_e)^2(n_h - n_e)^2 + (n_e \mu_e + n_h \mu_h)^2} \end{aligned} \quad (3)$$

The dashed curve in Fig. 7d shows that the CPMR data $R(H)/R(0)$ for $H > H_s$ are well fitted by Eq. (3) with parameters listed in Table 1. In this comparison, we used a single variable prefactor: scaled the calculated $\rho(H)$ by about 10% to fit the measured $\rho_{ab}(H = 0)$ value because of a large uncertainty in the sample sizes and intercontact distance (as was mentioned above) which affect the measured absolute resistivity value. The fitting curve described by Eq. (3) in low fields is parabolic, but becomes less steep as field increases. We note that Eq. (3) is not applicable for transport across the layers, $\mathbf{j}||c$, since in the quasi two-dimensional systems it has a more complicated character, as discussed below.

To conclude this section: the two-band transport model of impurity scattering explains rather well the non-linear Hall resistance (at least, at low temperatures), and the positive magnetoresistance data for in-plane transport (at $H > H_s$, when CPMR is not masked by NIMR).

The same set of parameters (Table 1) provides reasonable fitting of $R_{xy}(H)$, $\rho_{xx}(H=0)$, and $\delta R_{xx}(H)$ data for different samples and for the exfoliated flake. This suggests that no other mechanisms are required for describing, in the first approximation, the in-plane transport behavior.

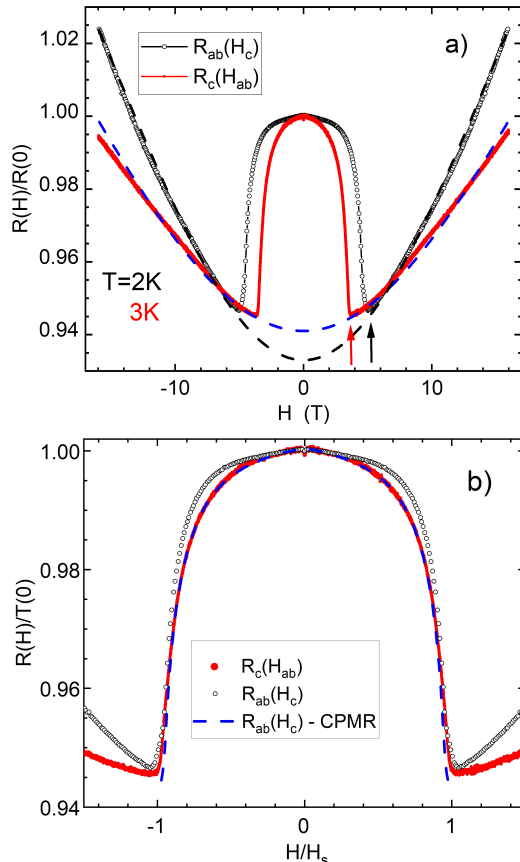


FIG. 9. (a) Normalized magnetoresistance for the bulk crystal in various geometry: red dots - $R_c(H\parallel ab)$, black open circles - $R_{ab}(H\parallel c)$, dashed blue and black lines - the CPMR fitting with a simplified parabolic $(\mu H)^2$ dependences. Vertical arrows indicate H_s for two field orientations. (b) The same normalized $R_c(H_{ab})$ (open circles) and $R_{ab}(H_c)$ (red dots) dependences vs normalized field H/H_s . The blue dashed curve shows the latter dependence from which the fitting PMR parabolic curve is subtracted.

Unconventional charge transport in c -direction, across the layers. The above text-book formula (3) derived for closed electron trajectories and for isotropic scattering is not applicable to the interlayer magnetotransport (i.e. R_c) in a field $H\parallel ab$. Indeed, if one applies formally the same Eq. (3) for CPMR in the $R_{ab}(H_c)$ and $R_c(H_{ab})$ configurations, the extracted values of an effective mobility μ^{eff} would differ by 0.5% only. This is clearly seen in Fig. 9b, where the prefactors of the parabolic $(\mu H)^2$ dependence for $R_c(H)$ and $R_{ab}(H)$ differ by 0.015%. Such minor difference of mobilities (along and across the layers) is in a striking contrast with the factor of 130 anisotropy in zero-field resistivity measured

along and across the ab plane (see Fig. 2).

For the $R_c(H_{ab})$ configuration one expects a crossover from a parabolic (in low field) to linear (in high field) MR [43–45] and can approximately use Eq. (34) of Ref. [44]. Even more surprising may look Fig. 7a that shows a non-zero CPMR for bias current along the field, $\mathbf{j}\parallel\mathbf{H}\parallel c$. Similar longitudinal interlayer magnetoresistance was also observed in many other quasi-2D metals being their general feature [46–49]; it was explained and described a decade ago [49–51]. These two facts indicate that charge transport across the layers in crystals with highly anisotropic conduction has a more complex character, where the carriers, moving on average in the c direction, propagate also along the highly conducting ab planes and experience therefore action of the perpendicular magnetic field. This interesting issue is however beyond the scope of the current paper.

3. Negative magnetoresistance

As we mentioned above, there are two qualitatively different types of the NIMR field dependence. Data of the 1st type (see Figs. 8, 9) is almost parabolic $\delta R(H)/R(0) \propto -aH^2$. The 2nd type NIMR (call it “flattened”) is more flat in low fields (Figs. 7) a,b,c.

The approximately parabolic shape of NIMR in the 1st type samples is similar to that observed earlier on EuSn_2As_2 in Refs. [5, 11]. On the other hand, the flattened type NIMR for EuSn_2As_2 may be seen in Ref. [10]. Comparing our results on EuSn_2As_2 with those measured on vdW AFM sister materials EuSn_2P_2 [15] and EuFe_2As_2 [4, 16], we also find qualitative similarity between NIMR in all these materials.

More detailed measurements [29] of magnetoresistance performed with various exfoliated flakes confirmed that NIMR is independent of the sample thickness. This evidences that NIMR does not originate from large-scale macroscopic lattice defects (such as misfit dislocations, domains, misoriented grains), and on the sample ab -plane bending. Indeed, these imperfections would be different for the bulk crystal and for exfoliated flakes. More detail on the XRD structural sample investigation is given in Supplemental materials [28].

Influence of the geometry of measurements on NIMR.

One of the reasons for the non-universality of NIMR is the obvious dependence of CPMR on the sample mobility μ that is anisotropic in layered crystals. The flattening, therefore, depends on the charge transport and field directions: the flattening is stronger for $R_{ab}(H_c)$, weaker for $R_c(H_{ab})$ - see Fig. 9, and is the weakest for $R_{ab}(H_{ab})$ - see Fig. 8, because CPMR is missing for $\mathbf{j}\parallel\mathbf{H}\parallel ab$.

In Fig. 9a we compare magnetoresistance measured on the same sample in different configurations: $R_{ab}(H\parallel c)$ (showing the most strong flattening) and $R_c(H\parallel ab)$. After subtracting CPMR from the original data, and normalizing magnetic field H/H_s (note, $H_s^{(ab)}$ and H_s^c are different- see Fig. 5) the two resulting curves in Fig. 9b

almost coincide; their proximity demonstrates that the configuration-dependent part of the flattening is mainly caused by a different classical parabolic CPMR (Eq. 3). In other words, NIMR develops on top of the background CPMR. In the configuration $R_{ab}(H||ab)$, where the positive MR is missing, NIMR looks closest to parabolic.

In agreement with the above arguments, we conclude that the parabolic-type NIMR, $\delta R(H) \propto -[M(H)]^2 \propto -H^2$, to be the *generic type dependence* for the layered AFM crystals. In Appendix A we present scaling analysis of the two types of NIMR and provide additional arguments in favor of this conclusion. We also discuss potential mechanisms for a sample-dependent departure of NIMR from the generic parabolic dependence. Searching for the potential origin of different types of NIMR, we performed detailed XRD, and transmission electron microscopy (TEM) examination of our samples, and precise magnetization measurements in low-field. For testing potential non-trivial topological order, suggested in [9], we also performed ARPES measurements supplemented with DFT band structure calculations. This information is presented in Appendices to our paper.

VI. THEORETICAL DESCRIPTION OF NEGATIVE ISOTROPIC MAGNETORESISTANCE IN LAYERED CONDUCTORS WITH AFM ORDER

Searching for an explanation for the observed NIMR, we analyzed the known MR mechanisms which might be potentially relevant to the studied case and found none to be able to explain the observed NIMR (see Ref. [23] and also Appendix B).

As we demonstrated in Fig. 12, NIMR is universal when plotted versus normalized magnetic field $\delta R(H/H_s)$; in other words, $\delta\rho(H) = \delta\rho[M(H)]$. Furthermore, $\delta\rho(M)$ is fully *isotropic* with respect to the field and current direction. This is in a sharp contrast with such well known effects as giant magnetoresistance (GMR), where the negative magnetoresistance is *anisotropic* (for more detail, see Appendix B). The observed isotropy of NIMR suggests the conventional short-range scattering by point-type defects [52]. From the fact that NIMR develops in the AFM state solely and is tied to magnetization field dependence, it follows that the electron scattering rate diminishes as spin polarization of Eu-atom layers changes from AFM- to FM-type. In contrast, ordinary scattering on magnetic impurities and magnons in the AFM metals and in AFM structures results in the positive MR (for more detail, see Appendix B).

A. Theoretical model and results

Very recently, the novel so-called exchange splitting mechanism of negative magnetoresistance in layered an-

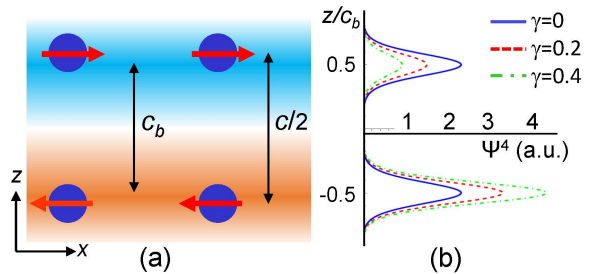


FIG. 10. Schematic illustration of the difference between spin-up and spin-down electron density distribution along the z -axis, represented by color intensity (orange – positive, blue – negative), in the half-cell of the $c/2$ -size. $c_b \approx c/2$ denotes the distance between two maxima of electron spin density. Dark blue circles show the Eu-atoms, and arrows - their magnetization direction in the AFM state.

tiferromagnetic semimetals has been proposed [23] to explain this effect in EuSn_2As_2 . Qualitatively, this mechanism can be understood as follows.

The conduction electrons originate from double layers of SnAs confined between the layers of Eu atoms (see Figs. 1a and VIA). The A-type AFM ordering of Eu spins doubles the lattice constant along the inter-layer z -direction and violates the binary \hat{Z}_2 symmetry between two adjacent Eu layers for each spin component σ of conducting electrons. This \hat{Z}_2 symmetry violation changes the z -dependence of the electron wave function $\Psi_\sigma(z)$ in bilayers containing two Eu layers of opposite spin polarization or AFM magnetization \mathbf{L}_{AFM} . The schematic picture of the electron wave functions is shown in Fig. VIA. In the paramagnetic state the electron wave function $\Psi_\sigma(z)$ is symmetric to the permutation $1 \leftrightarrow 2$ of two layers within the bilayer for each spin component σ . The AFM order reduces the electron energy of exchange interaction with Eu magnetic moment on one of these two layers and increases this energy on the other. It squeezes the electron wave function $\Psi_\sigma(z)$ toward the layer of lower energy. The electron scattering rate by short-range impurities or other crystal defects in the Born approximation is proportional to the fourth power of electron wave function [52]

$$1/\tau \propto \int |\Psi_\sigma(z)|^4 dz, \quad (4)$$

because it contains the square of matrix element $T_{\mathbf{n}'\mathbf{n}}^{(i)} = \int d^3\mathbf{r} \Psi_{\mathbf{n}'}^*(\mathbf{r}) V(\mathbf{r}) \Psi_{\mathbf{n}}(\mathbf{r})$ of electron scattering by disorder potential $V(\mathbf{r})$ between the quantum states \mathbf{n} and \mathbf{n}' . The compression of electron wave function $\Psi_\sigma(z)$ induced by bilayer \hat{Z}_2 symmetry violation increases the integral in Eq. (4), proportional to the electron scattering rate and metallic resistivity. Hence, the electric resistivity is larger in the AFM state than in paramagnetic. This enhancement requires a short correlation length of the scattering potential $V(\mathbf{r})$, shorter than the lattice constant in z -direction doubled by AFM order, which is

typical for impurities and other point crystal defects responsible for residual resistivity.

The negative magnetoresistance in the AFM state appears because of the field dependence of AFM order parameter \mathbf{L}_{AFM} . An external magnetic field \mathbf{H} tilts the spins of neighboring Eu layers towards \mathbf{H} , giving the field-induced magnetization $\mathbf{L}_{\parallel} = \chi\mathbf{H}$ along the magnetic field $\mathbf{L}_{AFM}(0)$. Hence, it reduces the antiferromagnetic vector \mathbf{L}_{AFM} approximately according to the classical relation

$$L_{AFM}(H) \approx \sqrt{L_{AFM}^2(0) - (\chi H)^2}. \quad (5)$$

Taking the magnetic susceptibility in AFM state $\chi(H) \approx const$, in agreement with the textbook behavior [53] and with experimental data for EuSn₂As₂ in our Fig. 5 and in other papers, we obtain:

$$L_{AFM}(H) \approx L_{AFM}(0) \sqrt{1 - (H/H_s)^2}, \quad (6)$$

Here H_s is the field of complete spin polarization, $H_s \approx 4\text{T}$ in EuSn₂As₂. Since the exchange term in electron energy $\Delta E_{ex} \propto L_{AFM}$,

$$\Delta E_{ex}(H) \approx \Delta E_{ex}(0) L_{AFM}(H)/L_{AFM}(0), \quad (7)$$

the bilayer wave-function asymmetry and spatial confinement also decrease quadratically in a low magnetic field $H < H_s$. This leads to a parabolic negative magnetoresistance almost up to the full spin polarization point H_s . At $H \rightarrow H_s$ the enhanced critical fluctuations are expected to make the second-order phase transition sharper and lead to a faster decrease of $L_{AFM}(H)$ than in the mean-field approximation described by Eq. (6).

The distinct feature of this mechanism of negative magnetoresistance is its almost complete isotropy to the magnetic field and electric current directions. The minor anisotropy to the field directions appears because of the anisotropic field dependence of AFM order parameter $L_{AFM}(\mathbf{H})$ due to magnetic anisotropy and the spin-flop transition. As shown in Ref. [23], the relative increase of resistivity due to the AFM ordering and NIMR effect is

$$\frac{\delta\rho(H)}{\rho(0)} \approx \frac{\gamma^2}{1 + 2\gamma^2}, \quad (8)$$

where the field-dependent ratio

$$\gamma = \gamma(H) = \frac{\Delta E_{ex}(H)}{2t_0} \approx \frac{\Delta E_{ex}(0)}{2t_0} \sqrt{1 - \frac{H^2}{H_s^2}} \quad (9)$$

of the exchange splitting energy ΔE_{ex} of conducting electrons to their hopping amplitude t_0 between the opposite AFM sublattices describes the degree of \hat{Z}_2 -symmetry violation between AFM sublattices and, hence, can be called the asymmetry parameter. From Eqs. (8) and (9) we see that at small $\gamma \ll 1$ and not very strong field

$H \ll H_s$ the NIMR correction is quadratic in magnetic field.

$$\frac{\rho(H) - \rho(0)}{\rho(0)} \approx \frac{\gamma^2(H) - \gamma^2(0)}{1 + 2\gamma^2(0)} \approx -\frac{H^2}{H_s^2} \left(\frac{\Delta E_{ex}}{2t_0} \right)^2. \quad (10)$$

At $H > H_s$ the NIMR correction (8)-(9) disappears, and one returns to the usual classical positive magnetoresistance in multiband conductors due to impurity scattering, which is parabolic at low field when $\omega_c\tau \ll 1$:

$$\rho_{zz}^m(H)/\rho_{zz}^m(0) = 1 + \omega_c^2\tau^2, \quad \omega_c\tau \ll 1, \quad (11)$$

where $\omega_c = eH/(m^*c)$ is the cyclotron frequency. Combining Eqs. (8) and (11) gives the schematic MR curve illustrated in Fig. 11 in agreement with experimental data.

Note that the AFM does not violate the symmetry $\hat{Z}_2 \cdot \hat{\theta}$, where $\hat{\theta}$ is the time reversal, which changes the spin projection σ . However, there is a protection of electron scattering to the opposite-spin states by a potential disorder, similar to the protection of chiral edge states to backscattering in topological insulators.

B. Rough theoretical estimates of maximal NIMR effect in EuSn₂As₂

The conduction electrons in EuSn₂As₂ come from SnAs bilayers. Below the Neel temperature T_N in A-type antiferromagnet, the two layers within one bilayer feel opposite magnetization of Eu spins from the nearest spin-polarized 2D Eu planes. The corresponding Zeeman-exchange spin-splitting in EuSn₂As₂ is $\Delta E_{ex} \approx 30 - 40\text{meV}$, as follows from the estimate based on our band-structure calculations in a ferromagnetic state [39].

The interlayer transfer integral t_0 in EuSn₂As₂ is more difficult to determine. Unfortunately, the ARPES data [9] do not have sufficient energy resolution to measure the bilayer splitting and t_0 directly. The t_0 value can only be roughly estimated from the observed resistivity anisotropy at low temperature $\rho_{zz}/\rho_{xx} \approx 130$ (see Fig. 2) and the width of in-plane energy band $4t_x \approx 1.9\text{eV}$, which is taken from our ARPES data and from the DFT calculation. As a result, we obtain the estimate $t_0 \approx t_x \sqrt{\rho_{zz}/\rho_{xx}} \approx 42\text{meV}$. Hence, the parameter $\gamma(0) = \Delta E_{ex}/(2t_0) \approx 0.36$, which according to Eq. (8) gives the maximal NIMR effect $\delta\rho(H)/\rho(0) \approx 0.1$ in EuSn₂As₂.

The observed NIMR effect is somewhat smaller than our theoretical prediction. For the longitudinal geometry $R_{ab}(H_{ab})$, which does not have a large contribution from positive MR, $\delta\rho(H)/\rho(0) \approx 0.06$ (see Fig. 11). The difference $\approx 4\%$ between the experiment and the above theoretical estimate comes because of (i) too rough theoretical estimates of ΔE_{ex} and t_0 and (ii) idealized theoretical model leading to Eqs. (8)-(9).

According to Eqs. (8)-(9) the NIMR effect depends quadratically on $\gamma(0) = \Delta E_{ex}/(2t_0)$, and reducing this ratio by 15 - 20% gives a good agreement between our

theoretical model and experiment. Another possible source of error in our calculations comes from the assumption of negligible overlap of wave functions ψ_1 and ψ_2 (see Eqs. (C3) and (C5) in Appendix C) and assumed in the derivation of Eq. (C12). A finite value at $z = 0$ of the wave function in Fig. 14 indicates that this overlap is nonzero. This assumption also leads to the overestimation of NIMR effect in Eq. (8) and its deviation from experimental data.

The exchange splitting mechanism of negative magnetoresistance corresponds to the energy scale $\Delta E_{ex} \approx 30 - 40$ meV that is much larger than the usual Zeeman splitting and temperature T . Hence, it is rather robust and should appear in many other compounds. However, in most AFM metals the effect is small by the parameter γ^2 as described in Eq. (8).

C. On the temperature dependence of NIMR

At low temperatures $T < T_N \ll \Delta E_{ex}$ in the AFM state, the main effect of finite temperature on the proposed NIMR mechanism is not on its magnitude but on the field H_s of complete spin polarization and, hence, on the magnetic-field width of the NIMR hump. According to the mean-field theory, one expects that the NIMR interval $H < H_s$ shrinks quadratically as temperature increases, $\Delta H_s(T)/H_s(0) = H_s(T)/H_s(0) - 1 \propto -(T/T_N)^2$. However, the fluctuations may modify this oversimplified $\Delta H_s(T)$ dependence, and their theoretical study is beyond the scope of our paper.

VII. QUANTITATIVE COMPARISON OF THE MEASURED MAGNETORESISTANCE WITH THEORY

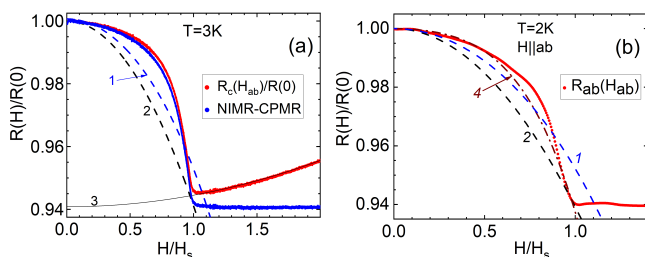


FIG. 11. Normalized magnetoresistance $R(H)/R(0)$ vs normalized magnetic field H/H_s . (a) Red dots - $R_c(H_{ab})$ at $T = 3$ K, blue dots - same data with subtracted CPMR. (b) Red dots $R_{ab}(H_{ab})$ at $T = 2$ K. Solid curves 1 - theoretical dependence with $\gamma(0) = 0.23$ evaluated as described in the text. Parabolas 2 are guide to the eye, matching the data at $H = H_s$. Solid line 3 - CPMR. Curve 4 - the 4th order fitting polynomial.

A. Negative magnetoresistance

In Figure 11 we compare the calculated negative magnetoresistance $R(H)/R(0)$ with the experimental data from Figs. 9, and 8 at the lowest temperature. One can see that the theoretical dependence (Eqs. (8) and (9)) reasonably well corresponds the measured NIMR after subtracting PMR from the raw $R(H)/R(0)$ data. The theoretically estimated prefactor value $\gamma(H = 0) = 0.23$ is consistent with a sample parabola (curve 1 in Fig. 11a) within 4%. Taking into account the large uncertainty in the ΔE_{ex} and t_0 values, the agreement between the theoretical and experimental parabolic prefactor values seems satisfactory.

Three notes should be made here. Firstly, as we mentioned above, in the vicinity of the phase transition (AFM-PM), the $R(H)$ dependence is expected to become steeper than Eq. (9) suggests. The sample curve 4 illustrates that the agreement may be improved when the 4th order terms are included.

Secondly, in Appendix A we show that flattening of the low field NIMR data (i.e., deviation from parabola in low fields) may be caused by magnon scattering. The latter produces an extra PMR term that quickly decays as $H \rightarrow H_s$, because magnons develop in the AFM state solely.

Thirdly, our scaling analysis of NIMR (see Appendix A 2) reveals a universal temperature dependence of $R(H/H_s)$ via $[H_s(0)/H(T) - 1] \propto T^\xi$ with $\xi \approx 2.5$. The simple mean-field arguments suggest a $H_s \propto T^2$ dependence. The empirical result might therefore be useful for future refined theoretical consideration.

VIII. CONCLUSIONS

The major aim of our studies was to clarify the origin of the *negative* magnetoresistance observed in layered non-Weyl AFM semimetals.

(1) In this paper we presented results of comprehensive magnetotransport measurements with EuSn_2As_2 , a typical representative material of this class. The considered materials demonstrate a negative magnetoresistance $R(H)$, firmly linked with magnetization $M(H)$ changes. The distinctive feature of NMR in these materials is its full isotropy with respect to the magnetic field and current directions. In order to distinguish this NMR from other known types of NMR (such as GMR and CMR), we called it “negative isotropic magnetoresistance” (NIMR). Our results give a strong evidence that NIMR in the layered AFM semimetals is an intrinsic property, almost irrelevant to defects, domains, and other sample-specific disorder.

(2) We explored in detail the novel magnetoresistance mechanism suggested in [23], and compared it with experimental data. In the proposed theory, the magnetoresistance primarily originates from exchange splitting of the energy levels of charge carriers confined between

differently polarized layers of Eu magnetic ions in the host lattice. Other, more conventional mechanisms, such as electron scattering by magnons and by staggered layered magnetization, play a secondary role. The combination of these mechanisms may explain a certain sample-dependent variation of the measured NIMR in the AFM state.

(3) Studying temperature dependence of NIMR, we have shown that whereas the magnitude of the NIMR hump is roughly T -independent in the AFM-domain of temperatures, the width of the $R(H)$ -hump in magnetic field, $\Delta H(T) \approx H_s(T)$, shrinks with temperature as $[H_s(0)/H_s(T)] - 1 \propto T^\xi$ with $\xi = 2.5$. This exponent differs somewhat from the above theoretical estimate $\xi = 2$ (sec. VIC), due to the oversimplified character of the mean mean-field model.

It might be that taking account of electron-electron interaction in short-range scattering may improve agreement with theory. Indeed, this mechanism produces the square root temperature dependence of the *positive* MR, $\delta\rho(H, T) \propto (\omega_c\tau)^2(T\tau)^{-1/2}$, in the ballistic interaction regime $T\tau \gg 1$ [54, 55]); the latter leads to broadening of the observed hump with temperature increasing. Detailed investigation of this issue is however beyond the scope of our paper.

(4) We have also shown that the *positive* magnetoresistance which is always observed (for current perpendicular to magnetic field direction) in layered AFM materials above the field of complete polarization, is described by conventional impurity scattering in a two-band system, $\delta R(H)/R(0) \propto (\mu^{\text{eff}}H)^2$. We have shown that the two-band model with the same parameters describes also quantitatively the non-linear field dependence of the Hall resistance. (For transport across the layers the classical positive MR may be described by Eq. (34) of Ref. [44].)

(5) The proposed mechanism of negative magnetoresistance is isotropic with respect to the directions of both the magnetic field and electric current, in agreement with our experiment. The magnitude of NIMR effect, estimated in Eqs. (8)-(9), is in a good agreement with experiment either.

(6) The presented ARPES data and DFT calculations confirm the multi-band energy spectrum with major contribution from the hole and electron bands around the Γ point. This agrees with the measured nonlinear magnetic field dependence of the Hall voltage.

(7) Our DFT calculations reveal the exchange splitting of the Sn-5 states in the AFM-ordered phase, and provide solid ground for our theory of the negative isotropic magnetoresistance [23]. The calculated exchange splitting of the energy levels enables to estimate the prefactor of the theoretical field dependence of NIMR, which appears to be in a good agreement with experimental data.

IX. ACKNOWLEDGEMENTS

AVS, OAS, KSP, and VMP acknowledge support from RSCF grant #23-12-00307.

Appendix A: Anatomy of the Magnetoresistance

The normalized negative magnetoresistance $\delta R(H)/R(0)$ has the same magnitude for the samples showing “parabolic” and “flattened” type magnetoresistance. The following pattern is worth noting: the observed flattening is stronger for $R_{ab}(H_c)$ and for $R_c(H_c)$ than for $R_{ab}(H_{ab})$. In Figure 9b we demonstrate that this difference is mainly due to the mobility anisotropy, and after subtracting the corresponding CPMR contribution, the $R(H)$ dependence becomes isotropic for one and the same crystal.

Besides this configuration-dependent regularity, there is also a sample-dependent flattening, which we associate with magnon scattering.

1. “Parabolic” and “Flattened” -type negative magnetoresistance in the AFM state

The difference in functional dependences of NIMR is most clearly pronounced at the lowest temperatures (cf Figs. 7 and 8). The measured nearly-parabolic NIMR shown in Fig. 11 in low fields $H \ll H_s$ looks qualitatively similar to the theoretical dependence $\delta R(H) \propto -H^2$ [23]. Deviations from the parabolic dependence were mentioned in Sections VI, VII) and might be a consequence of the proximity to the 2nd order phase transition at $H = H_s$. Below, we analyze a potential alternative origin of the $R(H)$ shape flattening.

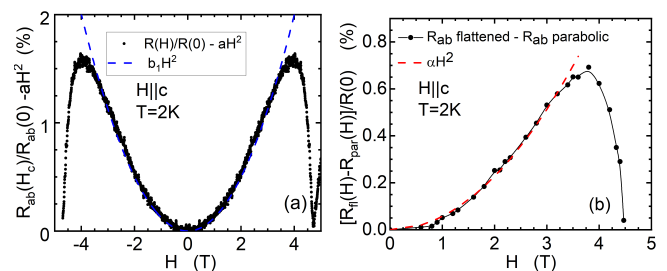


FIG. 12. (a) Example of the deviation of the measured $R_{ab}(H||c)$ dependence from the true parabola ($-aH^2$) with the prefactor a adjusted to fit the data at $H = H_s$ (see Fig. 11). (b) Difference in the magnetoresistance $R_{ab}(H||c)$ between the “flattened” and “parabolic” type samples. Dashed curve - (b_2H^2) with adjustable prefactor b_2 .

An example of the deviation ($R_{ab}(H) - aH^2$) for the “parabolic-type” sample is shown in Fig. 12a. For this analysis, the prefactor a is chosen to fit the data at $H = H_s$. Above $\approx 0.85H_s$ the deviation sharply vanishes.

In Figure 12b we plotted the difference between $R_{ab}(H)/R(0)$ for the representative 1st and 2nd type samples in the $H||c$ geometry where the difference is most pronounced.

One can see that the “flattened” type NIMR differs from the “parabolic” NIMR also by an extra positive MR term: the latter is two times less, it is very similar to the one shown in Fig. 12a. We conjecture that all positive contributions to MR in the AFM state originate from carrier scattering by magnons in the AFM crystal, and/or by randomly staggering layers magnetization. The former mechanism is universal, whereas the latter - sample dependent. Both PMR terms in the AFM state vanish sharply in fields above $0.8 \times H_s$.

The most important result is that in lower fields, the deviation by itself is parabolic in field as Figs. 12a,b show. This means, in particular, that there are no exponential-type hopping or temperature activated contributions to NIMR, and, respectively, no over-a-barrier type potential scattering mechanisms, like Kondo-scattering.

2. Scaling analysis of the negative magnetoresistance in the AFM state

In order to test whether the two different types of NIMR have a common or different physics behind, we performed their scaling analysis. Figures 13a and 13b show that the normalized magnetoresistance data taken at various temperatures for either type NIMR may be collapsed onto a single curve when field is scaled with a single scaling parameter $\zeta(T) = H(T=0)/H(T)$. The curves at the lowest temperature, $T = 3\text{ K}$ and 2 K for panels (a) and (b), respectively, have been taken as a reference curve $R(H, T=0)$.

Remarkably, in both cases the scaling parameter has the same temperature dependence: $\zeta \propto (1+T^\xi)$; in other words, the width of the NIMR hump shrinks with temperature as $\Delta H \propto 1/(1+T^\xi)$ where $\xi = 2.5 \pm 0.2$. The scaling holds in the temperature range up to T_N . The similarity of the two scaling curves and identical $\zeta(T)$ critical indices for two types samples confirm that (i) the physics behind two types of NIMR is the same, and (ii) the difference between the two types of NIMR is due to a larger positive magnetoresistance contribution in the “flattened”-type, than in the “parabolic”-type NIMR.

To conclude this section: our scaling analysis demonstrates that negative magnetoresistance in the AFM A-type semimetals is composed of *two parabolic contributions of the opposite sign*. The major universal negative contribution is described by our theory (Eqs. (8), (9) and Ref. [23]), the minor sample-dependent positive contribution vanishes sharply when field approaches H_s .

Appendix B: Overview of the known mechanisms of MR in magnetically ordered systems.

In search of an alternative explanation for the observed NIMR, we tried on well known MR mechanisms which might be potentially relevant to the studied case and found none to be able to explain it.

1. In ferromagnetic oxides, such as $\text{Ln}_{1-x}\text{Ca}_x\text{MnO}_3$, the magnetoresistance is negative and also correlates with magnetization [56]: the magnetoresistance in this case is phenomenologically described as $R(H, T) \propto \exp[-M(H, T)/M_0]$ and is explained by polaronic hopping transport below the ferromagnetic ordering temperature T_c . The model of polaron hopping transport in insulating oxides is evidently inapplicable to the semimetallic and well conducting layered AFM semimetals (and particularly to EuSn_2As_2), and to the diffusive- rather than hopping-type transport.
2. Giant magnetoresistance. The observed parabolic NIMR, at first glance, is reminiscent of a giant magnetoresistance (GMR) [25] in Fe/Cr superlattices where resistance decreases as magnetization in the neighbouring Fe-layers turns with external field from antiparallel to parallel [27]. For a single Fe-Cr-Fe sandwich, GMR amounts to $\Delta R/R \sim 1.5\%$ [57], whereas for the multilayered superlattice it reaches about 50% [27]. For ideally smooth superlattices, GMR should develop in transport across the layers (CPP); its presence in real structures for transport along the layers (CIP) have been attributed to diffusive scattering of electrons due to interface roughness [27, 57], As result, GMR is anisotropic [58]. In contrast, in EuSn_2As_2 under study, and in other similar AFM semimetallic crystals, the layered structure consists of monolayers of Eu atoms located in the correct lattice sites whose “roughness” is absent, and the magnetoresistance is fully isotropic.

The key-experimental facts suggesting irrelevance of GMR/CMR phenomenon to the NIMR under study are as follow:

- fully isotropic NIMR (for current in-plane CIP, and perpendicular to the plane CPP, see Figs. 8, 9 and Fig. 4 of Ref. [23]). This fact immediately prompts the point-like scattering to be responsible, rather than scattering by anisotropic extended defects (phase separation, domain boundaries, etc.). In contrast, GMR is usually larger in CPP geometry than in CIP (see e.g., Fig.6 of Ref. [58]);
- independence of NIMR on the crystal thickness (60nm-0.5mm) (see Ref. [29]);
- the obvious absence of the interface roughness of atomic layers in single crystals (NB: the roughness is introduced to explain the in-plane magnetoresistance within GMR) [27, 58];

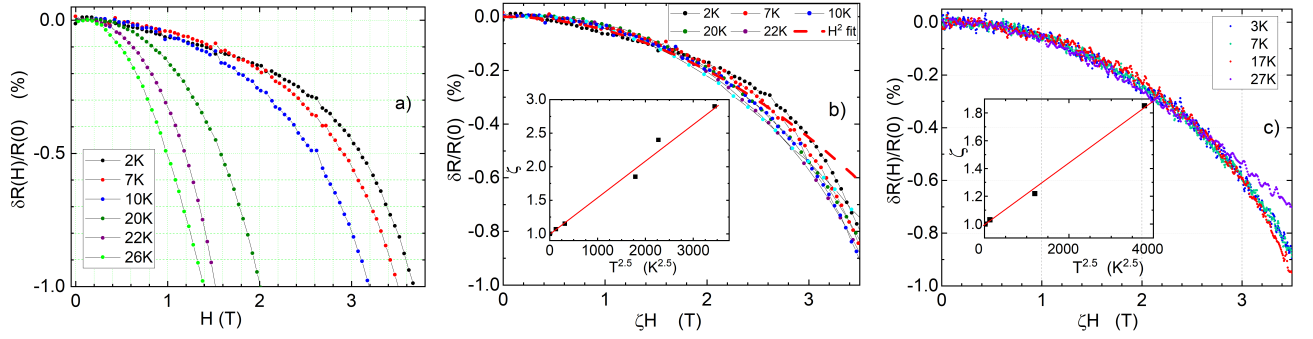


FIG. 13. Normalized negative magnetoresistance $\delta R(H, T)/R(0, 0)$: (a) Initial “flattened” type NIMR data from Fig. 7c. (b) Same “flattened” type NIMR data scaled versus $H^* = H(0)/\zeta(T)$ at various temperatures. (c) “Parabolic” type NIMR data scaled similarly. The insets show the scaling factor $\zeta(T)$ that is $\propto T^{2.5}$ for both plots.

- high quality lattice structure of the studied single crystals, the absence of grains and boundaries (confirmed by the precise XRD examination, and by the ARPES measurements of the energy band structure), and the absence of physical ground for phase separation effects.

- rather different temperature dependence of the width of NIMR hump. In the resistor network model for GMR and CMR [26] NMR scales as (H/T) . Hence, the GMR and CMR hump broadens as T increases, that is confirmed by numerous measurements (e.g., see Fig. 1 of [59], Fig. 4 of [26], and Fig. 3 of [13]).

In contrast, all experiments with layered AFM crystals show that the NIMR hump shrinks monotonically as temperature increases up to T_N (see Fig. 13a and Figs. 4 of [19], Fig. 5 of [15], Fig. 3b of [10], and Fig. 6b of [16]). Furthermore, the width of the NIMR hump scales as HT^ζ with $\zeta > 0$ (see Fig. 13).

-rather different shape of the magnetoresistance. NIMR for all studied compounds is convex in the range of temperatures up to T_N and fields up to H_s . By contrast, in the effective medium theory for doped perovskites [26], the curvature of the magnetoresistance is (H/T) -dependent and becomes concave-upward, concave-downward, and linear as H/T increases.

3. Anisotropic interlayer exchange between Eu moments has been conjectured for a sister compound, EuFe_2As_2 . There, the Fe moments are ordered in the striped SDW state and there is a biquadratic coupling between the Eu and Fe systems. In contrast, for EuSn_2As_2 , the magnetic system consists of Eu magnetic moments solely. - The half-filled $4f$ orbital of Eu^{2+} has zero orbital angular momentum ($L = 0$) and negligible single-ion anisotropy. For these reasons, the emergence of the in-plane anisotropy could not be expected and the anisotropy can hardly be an origin of NIMR for the wide class of materials listed above.

4. Electron-magnon scattering in antiferromagnets was considered theoretically in Refs. [60, 61], and for all relevant cases in the AFM state (i.e., at $T < T_N$ and $H < H_s$) was found to be *positive*. In particular, for $H \parallel$ easy axes (i.e. in our case, $H \parallel ab$ along the antiferromagnetic vector \mathbf{L}_{AFM}), in very low field below the spin flop field $H < H_{c1}$, and at low temperatures $\mu_B H_{c1} \ll T \ll T_N$:

$$\frac{\delta\rho(H)}{\rho(0)} \propto \left(\frac{H}{T}\right)^2, \quad (\text{B1})$$

where the spin-flop field H_{c1} is $\ll H_s$.

For another geometry, $H \perp$ easy axes (i.e., in our case, $H \perp$ easy magnetization ab plane), as temperature raises, the magnetoresistance changes from

$$\frac{\delta\rho(H)}{\rho(0)} \propto \left(\frac{T}{T_N}\right)^2 \left(\frac{H}{H_s}\right)^2 \quad \text{at } T \ll H \ll T_N, \quad (\text{B2})$$

to

$$\frac{\delta\rho(H)}{\rho(0)} \propto \left(\frac{T|H|}{T_N^2}\right) \quad \text{at } H \ll T < T_N.$$

Since $g\mu_B \approx 1.35 \text{ K/T}$, at the lowest temperature of our measurements $T \approx 2\text{K}$, Eq. (B3) is applicable in the field range from $\approx 2\text{T}$ to H_s . In any case, in the AFM state, resistance always *increases* with field because of a field-induced increase in spin fluctuations; this is in contrast to a suppression of the spin fluctuations in an external magnetic field for a ferromagnetic metal (see further).

The major theoretical results are confirmed by a large number of experimental studies, e.g. on antiferromagnetic Mn_2Au [62] and PrB_6 [63]. Since EuSn_2As_2 in the AFM state exhibits NIMR rather than PMR, we conclude this mechanism, at least, doesn't play a major role in NIMR.

5. Electron-magnon scattering in ferromagnets. The low temperature NMR was reported for ferromagnetic DyNiBC , GdNiBC , HoNiBC , and TbNiBC [64]. A strongly anisotropic NMR was

also observed in semiconductor GaAs nanowires “wrapped” in a ferromagnetic (Ga,Mn)As shell [65]. NMR in ferromagnets originates from the magnetic-field-induced suppression of magnon scattering that causes a sizable resistance decrease of several 10%. Functionally, at low temperatures $\Delta R(H)$ is almost linear for ferromagnetic boron carbides, $\Delta R(H) \propto -H$ [64], or concave for ferromagnetic GaAs/(Ga,Mn)As core-shell nanowires [65]. In all these cases of ferromagnet compounds, the $R(H)$ functional dependence is rather different from our case, Fig. 11, where it is always convex.

6. Kondo-scattering, i.e. the scattering of conduction electrons due to randomly located magnetic impurities. This scattering results in a characteristic minimum in electrical resistivity with temperature [66], due to an additional term $\rho(T) \propto \ln(\mu/T)$. In our case, firstly, no such a minimum or even a tendency is observed in Fig. 2. Secondly, there are no magnetic impurities in the stoichiometric EuSn_2As_2 compound grown from high purity raw materials.
7. Electron scattering by staggered magnetization. The XRD examination of the studied crystals (Supplemental materials [28]) revealed that the major type of the lattice defects is twisting the layers around the c -axis within $\pm 7^\circ$. We speculate that the intralayer FM-magnetization direction may somewhat stagger from layer to layer around the c axis, because magnetization may be tied to the crystal axes (a or b) by a second order in-plane anisotropy. This reason will cause a sample-dependent electron scattering.

Summarizing the above brief review, we conclude that none of the previously known mechanisms can explain the observed NIMR in the layered AFM semimetals. However, a minor sample-dependent positive contribution to MR in the AFM state might be related with either AFM magnon scattering, or with FM-static disorder.

The AFM order in defect-free samples and, hence, the magnon scattering are evidently universal. On the other hand, disorder pinning of the acoustic magnons is sample-dependent and may be a reason of the sample-dependent NIMR diversity. Alternatively, static spatial fluctuations of the magnetization direction due to the layers mis-orientation might be larger for samples with flattened-type NIMR. At the moment, however, we don't have either experimental verification of these possibilities, or a detailed theoretical description of the temperature and magnetic field-dependence of the scattering mechanism (and PMR).

Appendix C: Theoretical derivation of the negative isotropic magnetoresistance

1. Electron quantum states and wave functions in AFM metal

Let us consider the electron wave functions squeezing in the AFM state with a collinear and commensurate with lattice AFM order (see Figs. VIA and 14 for illustration). The two AFM sublattices are numerated by the index $i = 1, 2$ or by the “pseudospin” $\lambda = \lambda(i) = 3/2 - i$, while the projection of spin on the magnetization axis \mathbf{M}_{AFM} is denoted by index $\sigma = \pm 1 \equiv \uparrow, \downarrow$. The translation $\hat{T}_{\mathbf{A}}$ by the vector \mathbf{A} connects opposite AFM sublattices, and the product $\hat{T}_{\mathbf{A}}\hat{\theta}$ keeps the AFM crystal unchanged, where $\hat{\theta}$ is the time reversal operator. The quantum basis consists of four states, $|i, \sigma\rangle = \{1 \uparrow, 1 \downarrow, 2 \uparrow, 2 \downarrow\}$, corresponding to wave functions $\psi_{i,\sigma} = \{\psi_{1\uparrow}, \psi_{1\downarrow}, \psi_{2\uparrow}, \psi_{2\downarrow}\} = \psi_{i,\sigma}(\mathbf{r})$. By $\hat{T}_{\mathbf{A}}\hat{\theta}$ symmetry $\psi_{1\uparrow}(\mathbf{r}) = \psi_{2\downarrow}(\mathbf{r})$ and $\psi_{2\uparrow}(\mathbf{r}) = \psi_{1\downarrow}(\mathbf{r})$.

The usual Zeeman splitting $\Delta E_Z(\mathbf{H}) = (\vec{\sigma} \cdot \vec{\mathbf{H}}) g\mu_H/2$ in a relevant external magnetic field $H \lesssim 5\text{T}$ is much smaller than the exchange splitting $\Delta E_{ex} \gtrsim 10\text{meV}$ and will be neglected below. Then the AFM-sublattice part of the electron Hamiltonian for each electron quasi-momentum \mathbf{k} is given by the 4×4 matrix in the basis $|i, \sigma\rangle$, which decouples into two 2×2 matrices:

$$\hat{H}_\sigma = \begin{pmatrix} \Delta E_{ex}\sigma/2 & t_0 \\ t_0^* & -\Delta E_{ex}\sigma/2 \end{pmatrix}. \quad (\text{C1})$$

Here the non-diagonal term $t_0 = t_0^*$ is the intersublattice electron transfer integral. The diagonalization of Hamiltonian (C1) gives two eigenvalues

$$E_{\pm,\sigma} = \mp \sqrt{\Delta E_{ex}^2/4 + t_0^2} \quad (\text{C2})$$

and the corresponding wave functions (WF)

$$\psi_{\pm,\sigma} = \frac{\psi_1 (\sigma\gamma \pm \sqrt{\gamma^2 + 1}) + \psi_2}{\sqrt{1 + (\sigma\gamma \pm \sqrt{\gamma^2 + 1})^2}}, \quad (\text{C3})$$

where $\psi_{1,2}$ are the electron wave functions “localized” mostly on the first and second AFM sublattices and

$$\gamma = \Delta E_{ex}/2t_0 \quad (\text{C4})$$

the ratio of the exchange splitting ΔE_{ex} of conduction electron bands to their hopping amplitude t_0 between the opposite AFM sublattices, illustrated in Fig. ??.

Without the AFM order, i.e. at $\Delta E_{ex} = 0$, one gets the electron spectrum $E_{\pm,\sigma} = \mp t_0$ and the corresponding normalized eigenstates

$$\psi_{\pm,\sigma}^0 = (\psi_1 \pm \psi_2)/\sqrt{2}, \quad (\text{C5})$$

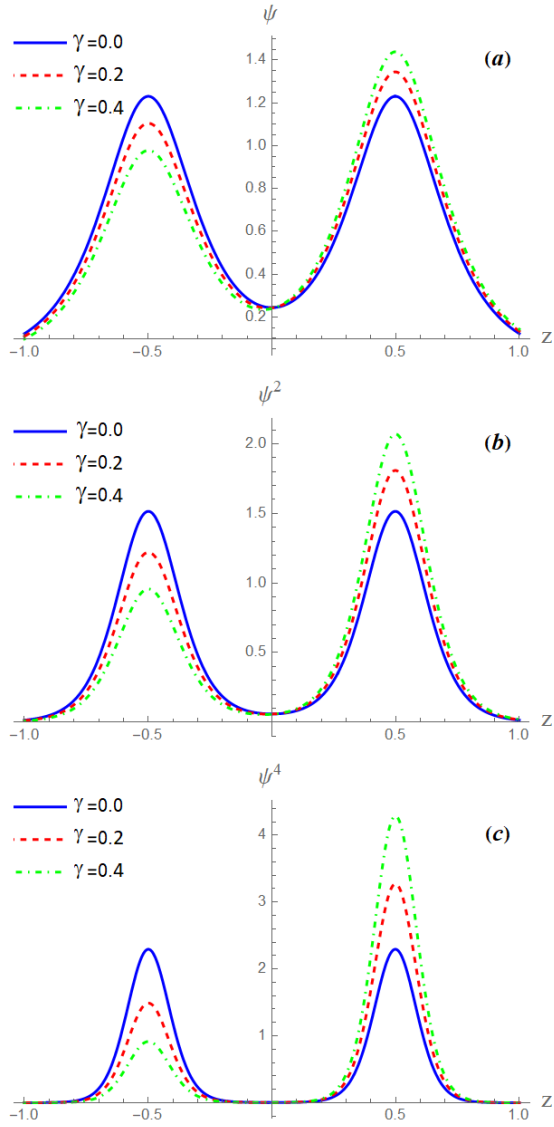


FIG. 14. Normalized electron wave function $\psi(z)$ (a) of the lowest-energy quantum state, given by Eq. (C3), in a bilayer, modeled by a double-well potential, its square $\psi^2(z)$ (b) and fourth power $\psi^4(z)$ (c). The asymmetry parameter $\gamma = \Delta E_{ex}/2t_z = 0$ (solid blue line), $\gamma = 0.2$ (dashed red line) and $\gamma = 0.4$ (dot-dashed green line). This figure illustrates the violation of \hat{Z}_2 symmetry of the electron wave function in bilayers due to the A-type AFM order and the enhancement of electron scattering rate proportional to $\psi^4(z)$ in Eq. (4).

which are symmetric and antisymmetric superpositions of electron states on sublattices 1 and 2, as it should be when the \hat{Z}_2 symmetry is conserved. From Eqs. (C3) we see that AFM lifts this symmetry, making the eigenfunction amplitude larger on one of two sublattices, as illustrated in Fig. 14. This enhances the integral in Eq. (4), as seen already from Figs. 14 and shown analytically below.

2. Mean free time in the Born approximation

In the Born approximation, i.e. the second-order perturbation theory in the impurity potential, the electron scattering rate is given by the Fermi's golden rule [52]:

$$\frac{1}{\tau} = \frac{2\pi}{\hbar} \sum_{n',i} |T_{n'n}^{(i)}|^2 \delta(\varepsilon_n - \varepsilon_{n'}). \quad (\text{C6})$$

where the index $n \equiv \{\mathbf{k}, \zeta, \sigma\}$ numerates quantum states, ζ and σ denote the electron subband and spin projection, ε_n is the electron energy in state n , and $\delta(x)$ is the Dirac delta-function. The short-range impurities or other crystal defects in solids are, usually, approximated by the point-like potential $V_i(\mathbf{r}) = U\delta(\mathbf{r} - \mathbf{r}_i)$. Here we omit the spin index σ because it is conserved by the potential scattering. The corresponding matrix element of electron scattering by this impurity potential is $T_{n'n}^{(i)} = U\Psi_{n'}^*(\mathbf{r}_i)\Psi_n(\mathbf{r}_i)$, where $\Psi_n(\mathbf{r})$ is the electron wave function in the state n .

For short-range impurities the matrix element does not depend on electron momentum \mathbf{k}' . Then the summation over \mathbf{k}' with the δ -function in Eq. (C6) gives the electron density of states (DoS) $\nu_{F\zeta} \equiv \nu_\zeta(\varepsilon_F)$ at Fermi energy ε_F per one spin component and per one subband ζ . The total DoS per one spin $\nu_F = \sum_\zeta \nu_{F\zeta}$. If the impurities are uniformly and randomly distributed in space, the sum over impurities rewrites as an integral over impurity coordinate: $\sum_i \rightarrow n_i \int d^3\mathbf{r}_i$, where n_i is the impurity concentration. Then Eq. (C6) becomes

$$\frac{1}{\tau} = \frac{2\pi}{\hbar} n_i U^2 \int d^3\mathbf{r}_i \sum_{\zeta'} \nu_{F\zeta'} |\Psi_{\mathbf{k}'\zeta'}^*(\mathbf{r}_i)\Psi_{\mathbf{k}\zeta}(\mathbf{r}_i)|^2. \quad (\text{C7})$$

The Bloch wave function is $\Psi_{\mathbf{k}\zeta}(\mathbf{r}) = \psi_\zeta(\mathbf{r}) \exp(i\mathbf{k}\mathbf{r})$, where $\psi_\zeta(\mathbf{r})$ is the periodic function. Then Eq. (C7) rewrites as

$$\frac{1}{\tau} = \frac{2\pi}{\hbar} n_i U^2 \nu_F I, \quad (\text{C8})$$

where the integral over one elementary cell

$$I \equiv \int d^3\mathbf{r} |\psi_\zeta(\mathbf{r})|^2 \sum_{\zeta'} \frac{\nu_{F\zeta'}}{\nu_F} |\psi_{\zeta'}(\mathbf{r})|^2. \quad (\text{C9})$$

For a single band ζ at the Fermi level, i.e. when $\nu_{F\zeta'} = 0$ for $\zeta' \neq \zeta$, this confirms Eq. (4). Eqs. (C8) and (C9) also result to Eq. (4) if only the scattering within the same band is allowed, e.g., due to the spin conservation during the potential scattering. Eqs. (C8),(C9) approximately give Eq. (4) also when there are several bands, but the DoS $\nu_{F\zeta}$ for one band ζ is much larger than that for the others. The latter happens in Dirac semimetals, where the DoS $\nu_\zeta(\varepsilon_F) \propto \varepsilon_F^{d-1}$ strongly depends on the Fermi energy ε_F and where the energy difference $\varepsilon_{\zeta'}(\mathbf{k}) - \varepsilon_\zeta(\mathbf{k}) \gtrsim \varepsilon_F$ for $\zeta' \neq \zeta$.

Now we estimate the difference δI of two integrals (C9) for the asymmetric and symmetric wave functions, given

by Eqs. (C3) and (C5). The host crystal lattice has the \hat{Z}_2 symmetry, therefore $\int \psi_1^4(z) dz = \int \psi_2^4(z) dz$. For simplicity, we also assume that the overlap of the wave functions on different AFM sublattices is negligible, i.e. $\psi_1\psi_2 \ll |\psi_1|^2$, and we neglect the products $\psi_1\psi_2 \approx 0$. The main conclusion remains valid also when $\psi_1\psi_2 \sim |\psi_1|^2$, but the calculation are more cumbersome.

First we consider the completely subband-polarized case $\nu_{F\zeta}/\nu_F = 1$ for $\zeta = 1$ and $\nu_{F\zeta}/\nu_F = 0$ for $\zeta = 2$. Then for the symmetric wave function (C5), corresponding to the lowest subband ζ without the AFM order and bilayer asymmetry, the integral (C9) is

$$I_0 = \int d^3\mathbf{r} |\psi_+^s|^4 dz \approx \int d^3\mathbf{r} \psi_1^4/2. \quad (\text{C10})$$

We now calculate the difference

$$\delta I \equiv I - I_0 = \int d^3\mathbf{r} (|\psi_+|^4 - |\psi_+^s|^4), \quad (\text{C11})$$

which gives the correction to mean free time τ according to Eq. (4) or (C8). After the substitution of Eqs. (C3) and (C5), at $\psi_1\psi_2 \ll |\psi_1|^2$ this simplifies to

$$\delta I \approx \frac{\gamma^2}{1 + \gamma^2} \int d^3\mathbf{r} \frac{\psi_1^4(z)}{2} = \frac{\gamma^2 I_0}{1 + \gamma^2} = \frac{\gamma^2 I}{1 + 2\gamma^2}. \quad (\text{C12})$$

Combining Eqs. (C12) and (C8) gives the decrease of the electron mean free time from the squeezing of electron wave function by AFM order and the corresponding enhancement of impurity scattering:

$$\frac{\delta\tau}{\tau_0} \approx -\frac{\delta I}{I_0} \approx \frac{-\gamma^2}{1 + \gamma^2}. \quad (\text{C13})$$

3. Negative isotropic magnetoresistance

Substituting Eqs. (C12), (C4) and (7) to (C8) we obtain the relative increase of resistivity due to the AFM ordering

$$\begin{aligned} \frac{\delta\rho(H)}{\rho(0)} &\approx -\frac{\delta\tau}{\tau} \approx \frac{\delta I}{I} \approx \frac{\gamma^2}{1 + 2\gamma^2} \\ &\approx \frac{[\Delta E_{ex}/(2t_0)]^2 (1 - H^2/H_s^2)}{1 + 2[\Delta E_{ex}/(2t_0)]^2 (1 - H^2/H_s^2)}. \end{aligned} \quad (\text{C14})$$

At $\gamma^2 \ll 1$ Eq. (C12) simplifies to $\delta I \approx \gamma^2 I_0 \approx \gamma^2 I$, and Eq. (C14) simplifies to

$$\frac{\delta\rho(H)}{\rho(0)} \approx \gamma^2 \approx \left(\frac{\Delta E_{ex}}{2t_0}\right)^2 \left(1 - \frac{H^2}{H_s^2}\right). \quad (\text{C15})$$

Contrary to the NMR caused by chiral anomaly in Weyl semimetals, this increase of resistivity is *isotropic*. For example, our NIMR mechanism applies both for the interlayer and in-plane current directions in layered conductors, and it only slightly depends on the magnetic field direction due to a magnetic anisotropy solely.

In usual 3D AFM metals the proposed NIMR mechanism is very weak, because the ratio $\gamma = \Delta E_{ex}/2t_0 \ll 1$. Indeed, $\Delta E_{ex} \lesssim 0.1\text{eV}$, while $2t_0 \sim 1\text{eV}$ is comparable to the bandwidth. However, in strongly anisotropic layered materials with A-type AFM order the ratio $\gamma = \Delta E_{ex}/2t_0 \sim 1$, because the interlayer transfer integral $t_0 \lesssim 0.1\text{eV}$ in van-der-Waals or other layered compounds is also small.

In strong magnetic field approaching the complete spin polarization (or spin-flip transition), at $H/H_s \approx 1$, the field dependence of magnetization L and exchange energy ΔE_{Zex} may differ from Eqs. (5) and (7). Because of fluctuations, the actual spin-flip transition is often sharper and is shifted to smaller fields than that given by the mean-field theory and Eq. (5). Then the magnetoresistance at $H \approx H_s$ also develops sharper than that described by Eqs. (C14) and (C15).

4. Contribution of the classical positive magnetoresistance: qualitative consideration

At $H > H_s$ the obtained correction (C15) disappears, and one returns to the usual positive magnetoresistance in multiband conductors due to impurity scattering, which is parabolic at low field when $\omega_c\tau \ll 1$ [52]:

$$\rho_{zz}^m(H) / \rho_{zz}^m(0) = 1 + \omega_c^2\tau^2, \quad \omega_c\tau \ll 1, \quad (\text{C16})$$

where $\omega_c = eH/(m^*c)$ is the cyclotron frequency. Here ω_c and τ refer to the carriers of the dominating band m . We highlight that the positive magnetoresistance $\gamma\rho_{ii} \propto (\omega_c\tau)^2$ is intrinsic to the multicomponent carrier system solely, since for the single-component system with isotropic spectrum ρ_{ii} does not depend on magnetic field up to $(\omega_c\tau)^4$. Therefore, the existence of the parabolic PMR by itself is in accord with our ARPES data and band structure calculations, which confirm the presence of the hole band at Γ point and the electron band at M point.

At $H < H_s$ both Eqs. (C15) and (C16) contribute to magnetoresistance. Combining Eqs. (C15) and (C16) gives the schematic MR curve at $H < H_s$:

$$\frac{\rho(H)}{\rho(0)} \approx 1 - \frac{(\Delta E_{ex}/2t_0)^2}{1 + 2(\Delta E_{ex}/2t_0)^2} \frac{H^2}{H_s^2} + [\omega_c(H)\tau]^2, \quad (\text{C17})$$

illustrated in Fig. 11, which resembles very much the experimental observations.

Below $H < H_s$ both the second and third terms are at work and compete, because both give the quadratic MR but of opposite signs. This is seen from the experimental data in Fig. 11, where the positive term of magnetoresistance depends on mutual orientation of the resistivity component R and magnetic field \mathbf{H} . The positive classical MR term is absent for longitudinal MR $R_{ab}(H_{ab})$, and the corresponding NIMR effect is indeed stronger for this geometry, as seen from Fig. 11. At $H \geq H_s$ when the AFM state converges to FM order, the second term in Eq. (C17) vanishes to zero, and MR becomes positive.

5. Generalizations

Similar qualitative idea should work not only for bilayer crystals with A-type AFM with wave vector across the layers, but also for any antiferromagnetic conductor. Indeed, in a commensurate AFM state the unit cell doubles as compared to nonmagnetic state. Hence, in the new doubled unit cell there are two electron states per each quasi-momentum, denoted by indices 1 and 2. These two states are degenerate without AFM, which we called the $\tilde{Z}_2 : 1 \leftrightarrow 2$ symmetry, but this degeneracy is lifted by AFM. Without AFM the electron wave function is given by a symmetric or antisymmetric superposition of these two states, as in Eq. (C5). In the AFM state this symmetry is lifted, as in Eq. (C3). Repeating the arguments given above we obtain that the integral in Eq. (C9) is greater in AFM state, i.e. when the $1 \leftrightarrow 2$ symmetry is lifted, so that the wave function $\Psi_{\mathbf{k}}(\mathbf{r})$ is more localized. This gives to extra resistance given by Eq. (C15), where t_0 is now the transfer integral between states 1 and 2, corresponding to electron hopping between two opposite AFM sublattices. However,

in most AFM metals this transfer integral t_0 is comparable to the bandwidth and much larger than $\Delta E_{Z_{ex}}$, so that the correction (C15) is negligibly small. However, if in a AFM conductor $(\Delta E_{Z_{ex}}/4t_0)^2$ is not too small, a quadratic negative magnetoresistance similar to that in EuSn_2As_2 may appear.

The performed theoretical analysis is, usually, applicable to both single-band and multi-band metals. If there are several electronic bands on the Fermi level, the scattering rate given by Eq. (C6) is also valid, but the sub-band index ζ now numerates the crystalline electronic bands each split into two subbands given by Eq. (C2). Then the integral (C9) also contains the sum over electronic bands on the Fermi level. If the values of parameters t_0 and $\Delta E_{Z_{ex}}$ are close for all electronic bands, the final result given by Eq. (C15) does not change.

Often, the impurity distribution within elementary cell is not uniform and described by a normalized distribution function $D(\mathbf{r}_i)$, $\int D(\mathbf{r}_i) d\mathbf{r}_i = V$. If the in-plane and interlayer coordinates in the electron wave function $u_{\mathbf{k}}(\mathbf{r})$ do not disentangle, e.g. for zigzag crystal structures, one should use Eq. (C7) instead of (C8). Then the formulas in the rest of this section are not as simple, but the qualitative result is still valid.

-
- [1] C. Z. Chang, J. S. Zhang, X. Feng, J. Shen, Z. C. Zhang, M. H. Guo, K. Li, Y. B. Ou, P. Wei, L. L. Wang, Z. Q. Ji, Y. Feng, S. H. Ji, X. Chen, J. F. Jia, X. Dai, Z. Fang, S. C. Zhang, K. He, Y. Y. Wang, L. Lu, X. C. Ma, and Q. K. Xue, Experimental Observation of the Quantum Anomalous Hall Effect in a Magnetic Topological Insulator $\text{Cr}:(\text{Bi,Sb})_2\text{Te}_3$, *Science* **340** 167 (2013).
- [2] D. Zhang, M. Shi, T. Zhu, D. Xing, H. Zhang, and J. Wang, Topological Axion States in the Magnetic Insulator MnBi_2Te_4 with the Quantized Magnetoelectric Effect *Phys. Rev. Lett.* **122**, 206401 (2019).
- [3] Na Hyun Jo, B. Kuthanazhi, Yun Wu, et al., Manipulating magnetism in the topological semimetal EuCd_2As_2 , *Phys. Rev. B* **101**, 140402(R) (2020)
- [4] J. J. Sanchez, G. Fabbris, Y. Choi, Yue Shi, P. Malinowski, S. Pandey, J. Liu, I. I. Mazin, Jong-Woo Kim, P. Ryan, and Jiun-Haw Chu, Strongly anisotropic antiferromagnetic coupling in EuFe_2As_2 revealed by stress detwinning, *Phys. Rev. B* **104**, 104413 (2021).
- [5] M. Q. Arguilla, N. D. Cultrara, Z. J. Baum, S. Jiang, R. D. Ross, J. E. Goldberger, EuSn_2As_2 : an exfoliatable magnetic layered Zintl-Klemm phase, *Inorg. Chem. Front* **4**, 378 (2017).
- [6] S. Pakhira, M. A. Tanatar, T. Heitmann, D. Vaknin, and D. C. Johnston, A-type antiferromagnetic order and magnetic phase diagram of the trigonal Eu spin-7/2 triangular-lattice compound EuSn_2As_2 *Phys. Rev. B* **104**, 174427 (2021).
- [7] I. A. Golovchanskiy, E. I. Maltsev, I. V. Shchetinin, V. A. Vlasenko, P. S. Dzhumaev, K. S. Pervakov, V. V. Emelyanova, A. Yu. Tsvetkov, N. N. Abramov, V. M. Pudalov, V. S. Stolyarov, Magnetic resonances in EuSn_2As_2 single crystal, *J. Magn. Magn. Mater.*, **562**, 169713 (2022)
- [8] X. Lv, X. Chen, B. Zhang, P. Jiang, and Zh. Zhong, Thickness-Dependent Magnetism and Topological Properties of EuSn_2As_2 , *ACS Appl. Electron. Mater.* **4**, 7, 3212 (2022).
- [9] Hang Li, Shun-Ye Gao, Shao-Feng Duan, Yuan-Feng Xu, et al., Dirac Surface States in Intrinsic Magnetic Topological Insulators EuSn_2As_2 and $\text{MnBi}_2\text{nTe}_{3n+1}$, *Phys. Rev. X* **9**, 041039 (2019).
- [10] Huan-Cheng Chen, Zhe-Feng Lou, Yu-Xing Zhou, Qin Chen, Bin-Jie Xu, Shui-Jin Chen, Jian-Hua Du, Jin-Hu Yang, Hang-Dong Wang, and Ming-Hu Fang, Negative Magnetoresistance in Antiferromagnetic Topological Insulator EuSn_2As_2 , *Chin. Phys. Lett.* **37**, No. 4, 047201 (2020).
- [11] H. Li, W. Gao, Z. Chen, W. Chu, Y. Nie, S. Ma, Y. Han, Min Wu, T. Li, Q. Niu, W. Ning, X. Zhu, and M. Tian, Magnetic properties of the layered magnetic topological insulator EuSn_2As_2 , *Phys. Rev. B* **104**, 054435 (2021).
- [12] Yuanfeng Xu, Zhida Song, Zhijun Wang, Hongming Weng, and Xi Dai, Higher-Order Topology of the Axion Insulator EuIn_2As_2 , *Phys. Rev. Lett.* **122**, 256402 (2019).
- [13] J. Fontcuberta, B. Martínez, A. Seffar, S. Piñol, J. L. García-Muñoz, and X. Obradors, Colossal Magnetoresistance of Ferromagnetic Manganites: Structural Tuning and Mechanisms, *Phys. Rev. Lett.* **76**, 1122 (1996).
- [14] G. M. Pierantozzia, A. De Vita, Chiara Bigia, et al. Evidence of magnetism-induced topological protection in the axion insulator candidate EuSn_2P_2 , *PNAS* **119**(4) e2116575119 (2022).
- [15] X. Gui, I. Pletikovic, H. Cao, et al., A New Magnetic Topological Quantum Material Candidate by Design,

- ACS Centr. Sci. **5**(5), 900 (2019).
- [16] S. Jiang, Y. Luo, Z. Ren, Z. Zhu, C. Wang, X. Xu, Q. Tao, G. Cao and Z. Xu, Metamagnetic transition in EuFe_2As_2 single crystals, *New J. Phys.* **11**, 025007 (2009).
- [17] I. A. Golovchanskiy, N. N. Abramov, V. A. Vlasenko, K. Pervakov, I. V. Shchetinin, P. S. Dzhumaev, O. V. Emelyanova, D. S. Baranov, D. S. Kalashnikov, K. B. Polevoy, V. M. Pudalov, and V. S. Stolyarov, Antiferromagnetic resonances in twinned EuFe_2As_2 single crystals, *Phys. Rev. B*, **106**, 024412 (2022).
- [18] Yu. I. Talanov, I. I. Gimazov, R. B. Zaripov, K. S. Pervakov, V. A. Vlasenko, V. M. Pudalov, and G. B. Teitelbaum, Study of the antiferromagnetic state nematics in EuFe_2As_2 by using spin-resonance and magnetic measurements, *JETP Letters* **117**(6), 470 (2023).
- [19] J. J. Ying, Y. J. Yan, A. F. Wang, Z. J. Xiang, P. Cheng, G. J. Ye, and X. H. Chen, Metamagnetic transition in $\text{Ca}_{1-x}\text{Sr}_x\text{Co}_2\text{As}_2$ ($x = 0$ and 0.1) single crystals, *Phys. Rev. B* **85**, 214414 (2012).
- [20] Jinhu Yang, Wuzhang Yang, Qingqin Zhu, Bin Chen, Hangdong Wang, Qianhui Mao, Jianhu Du, Zhefeng Lou, Minghu Fang, *J. Magn. Magn. Mater.* **474**, 50 (2019). Spin-flop transition and magnetic phase diagram in CsCo_2Se_2 revealed by torque and resistivity measurements
- [21] T. K. Kim, K. S. Pervakov, D. V. Evtushinsky, S. W. Jung, G. Poelchen, K. Kummer, V. A. Vlasenko, A. V. Sadakov, A. S. Usoltsev, V. M. Pudalov, D. Roditchev, V. S. Stolyarov, D. V. Vyalikh, V. Borisov, R. Valent?, A. Ernst, S. V. Ereemeev, E. V. Chulkov, Electronic structure and coexistence of superconductivity with magnetism in $\text{RbEuFe}_4\text{As}_4$, *Phys. Rev. B* **103**, 174517 (2021).
- [22] V. S. Stolyarov, K. S. Pervakov, A. S. Astrakhantseva, I. A. Golovchanskiy, D. V. Vyalikh, T. K. Kim, S. V. Ereemeev, V. A. Vlasenko, V. M. Pudalov, A. A. Golubov, E. V. Chulkov, and D. Roditchev, Electronic Structures and Surface Reconstructions in Magnetic Superconductor $\text{RbEuFe}_4\text{As}_4$ *J. Phys. Chem. Lett.* **11**, 9393-9399 (2020).
- [23] P. D. Grigoriev, N. S. Pavlov, I. A. Nekrasov, I. R. Shein, A. V. Sadakov, O. A. Sobolevskiy, E. Maltsev, N. Perez, L. Veyrat, and V.M. Pudalov, Exchange Splitting Mechanism of Negative Magnetoresistance in Layered AFM Semimetals. arXiv: 2405.18046
- [24] E. Dagotto, T. Hotta, A. Moreo, Colossal magnetoresistant materials: the key role of phase separation, *Phys. Rep.* **344**, 1 (2001).
- [25] Elbio Dagotto, *Nanoscale Phase Separation and Colossal Magnetoresistance*, Springer-Verlag, 2002.
- [26] Wei-Guo Yin, Ruibao Tao, Effective-medium theory of the giant magnetoresistance in magnetic granular samples and doped LaMnO_3 perovskites. *Phys. Rev.* **62**, 550 (2000).
- [27] M. N. Baibich, J. M. Broto, A. Fert, F. Nguyen Van Dau, F. Petroff, P. Etienne, G. Creuzet, A. Friederich, and J. Chazelas, Giant magnetoresistance of $(001)\text{Fe}/(001)\text{Cr}$ Magnetic Superlattices, *Phys. Rev. Lett.* **61**, 2472 (1988).
- [28] See Supplemental Material at [URL will be inserted by publisher] for more detailed information on the synthesis, XRD structural analysis, computational details of electron magnetotransport, electronic band structure (ARPES data and calculations).
- [29] E. I. Maltsev, L. Veyrat, N. R. Perez, R. Giraud, J. Dufouleur, and B. Büchner, K. S. Pervakov and V. M. Pudalov, Anomalous Hall Effect in EuSn_2As_2 Thin Flakes, to be published elsewhere.
- [30] D. P. Rojas, J. R. Fernandez, J. I. Espeso and J. C. Gómez Sal, Antiferromagnetic Kondo lattice behaviour of YbNiAl_2 alloy *J. Alloys Compounds* **502**, 275 (2010).
- [31] F. H. Yu, H. M. Mu, W. Z. Zhuo, Z. Y. Wang, Z. F. Wang, J. J. Ying, and X. H. Chen, Elevating the magnetic exchange coupling in the compressed antiferromagnetic axion insulator candidate *Phys. Rev. B* **102**, 180404(R) (2020).
- [32] S. Sakuragi, S. Sasaki, R. Akashi, R. Sakagami, K. Kuroda, C. Bareille, T. Hashimoto, T. Nagashima, Y. Kinoshita, Y. Hirata, et al., Spintronic superconductor in a bulk layered material with natural spin-valve structure. arXiv:2001.07991 (2020).
- [33] G. Kresse, J. Furthmüller, Efficient iterative schemes for ab initio total-energy calculations using a plane-wave basis set, *Phys. Rev. B*, **54**, 11169 (1996).
- [34] J. P. Perdew, K. Burke, M. Ernzerhof, Generalized Gradient Approximation Made Simple, *Phys. Rev. Lett.* **77**, 3865 (1996).
- [35] S. L. Dudarev, G. A. Botton, S. Y. Savrasov C. J. Humphreys, and A. P. Sutton, *Phys. Rev. B*, **57**, 1505 (1998).
- [36] L.-D. Yuan, Z. Wang, J.-W. Luo, and A. Zunger, Prediction of low-Z collinear and noncollinear antiferromagnetic compounds having momentum-dependent spin splitting even without spin-orbit coupling, *Phys. Rev. Materials* **5**, 014409 (2021).
- [37] D. MacNeill, J.T. Hou, D.R. Klein, P. Zhang, P. Jarillo-Herrero, L. Liu, Gigahertz Frequency Antiferromagnetic Resonance and Strong Magnon-Magnon Coupling in the Layered Crystal CrCl_3 , *Phys. Rev. Lett.* **123**, 047204 (2021).
- [38] A. G. Gurevich, Melkov G.A. (Eds.), *Magnetization Oscillations and Waves*, CRC Press, 1996.
- [39] A. Yu. Degtyarenko, A. L. Vasiliev, N. S. Pavlov, A. V. Ovcharov, V. I. Bondarenko, A. V. Sadakov, K. S. Pervakov, and V. M. Pudalov, Ferromagnetic Nano-defects in Antiferromagnetic EuSn_2As_2 Single Crystals. To be published elsewhere.
- [40] J. Yan, Z. Z. Jiang, R. C. Xiao, W.J. Lu, W. H. Song, X. B. Zhu, X. Luo, Y. P. Sun, and M. Yamashita. Field-induced topological Hall effect in antiferromagnetic axion insulator candidate EuIn_2As_2 , *Phys. Rev. Research*, **4**, 013163, (2022).
- [41] A. Yu. Kuntsevich, L. A. Morgun, and V. M. Pudalov, Electron-electron interaction correction and magnetoresistance in tilted fields in Si-based two-dimensional systems, *Phys. Rev. B* **87**, 205406 (2013). DOI: 10.1103/PhysRevB.87.205406
- [42] Hualei Sun, C. Chen, Y. Hou, Yu Gong, M. Huo, L. Li, J. Yu, W. Cai, N. Liu, R. Wu, D.-X. Yao, and M. Wang, Magnetism variation of the compressed antiferromagnetic insulator EuSn_2As_2 , *Sci. China*, **64**, No. 11, 118211 (2021).
- [43] P. Moses and R. H. McKenzie, Comparison of coherent and weakly incoherent transport models for the interlayer magnetoresistance of layered Fermi liquids, *Phys. Rev. B* **60**, 7998 (1999).
- [44] A. J. Schofield and J. R. Cooper, Quasilinear magnetoresistance in an almost two-dimensional band structure, *Phys. Rev. B* **62**, 10779 (2000).
- [45] P.D. Grigoriev, T.I. Mogilyuk, Angular dependence

- of magnetoresistance in strongly anisotropic quasi-two-dimensional metals: Influence of Landau-level shape, *Phys. Rev. B* **90**, 115138 (2014).
- [46] J. Wosnitza, Quasi-Two-Dimensional Organic Superconductors, *J. Low Temp. Phys.* **146**, 641 (2007).
- [47] M. V. Kartsovnik, P. D. Grigoriev, W. Biberacher, and N. D. Kushch, Magnetic field induced coherence-incoherence crossover in the interlayer conductivity of a layered organic metal, *Phys. Rev. B* **79**, 165120 (2009).
- [48] W. Kang, Y. J. Jo, D. Y. Noh, K. I. Son, and Ok-Hee Chung, *Phys. Rev. B* **80**, 155102 (2009).
- [49] P. D. Grigoriev, M. V. Kartsovnik, and W. Biberacher, *Phys. Rev. B* **86**, 165125 (2012)
- [50] P. D. Grigoriev, Weakly incoherent regime of interlayer conductivity in a magnetic field, *Phys. Rev. B* **83**, 245129 (2011).
- [51] P. D. Grigoriev, Longitudinal interlayer magnetoresistance in strongly anisotropic quasi-two-dimensional metals, *Phys. Rev. B* **88**, 054415 (2013).
- [52] A. A. Abrikosov, *Fundamentals of the theory of metals*, North-Holland, 1988.
- [53] C. Kittel, *Quantum theory of Solids*, J. Wiley & Sons, Inc. (1963).
- [54] I.V. Gornyi, A. D. Mirlin, Interaction-Induced Magnetoresistance: From the Diffusive to the Ballistic Regime, *Phys. Rev. Lett.* **90**, 076801 (2003).
- [55] N.N. Klimov, D.A. Knyazev, O.E. Omel'yanovskii, V.M. Pudalov, H.Kojima, M.E. Gershenson, Interaction Effects in Conductivity of a Two-Valley Electron System in High-Mobility Si Inversion Layers, *Phys.Rev. B* **78**, 195308 (2008).
- [56] M. F. Hundley, M. Hawley, R. H. Heffner, Q. X. Jia, J. J. Neumeier, J. Tesmer, J. D. Thompson, and X. D. Wu, Transport-magnetism correlations in the ferromagnetic oxide $\text{La}_{0.7}\text{Ca}_{0.3}\text{MnO}_3$, *Appl. Phys. Lett.* **67**, 860 (1995).
- [57] R. E. Camley and J. Barnas, Theory of Giant Magnetoresistance Effects in Magnetic Layered Structures with Antiferromagnetic Coupling, *Phys. Rev. Lett.* **63**, 664 (1989).
- [58] A. Barthelemy, A. Fert, F. Nguyen Van Dau, "Giant Magnetoresistance", *Encyclopedia of Materials: Science and Technology*, ISBN: 978-0-08-043152-9, p. 3521-3531 (2001).
- [59] C.Xu, Z.-Ya Li, *J. Phys.: Cond. Mat* **11**, 847 (1999).
- [60] H. Yamada, and S. Takada, Magnetoresistance of antiferromagnetic metals due to s-d interaction, *J. Phys. Soc. Jpn.*, **34**, 51 (1973).
- [61] H. Yamada, and S. Takada, Magnetoresistance due to Electron-Spin Scattering in Antiferromagnetic Metals at Low Temperatures, *Progress of Theor. Phys.* **49**, 1401 (1973).
- [62] S. Yu. Bodnar, Y. Skourski, O. Gomonay, J. Sinova, M. Kläui, and M. Jourdan, Magnetoresistance Effects in the Metallic Antiferromagnet Mn_2Au , *Phys. Rev. Applied*, **14**, 014004 (2020).
- [63] Naushad Ali, S. So Woods, Magnetoresistance of antiferromagnetic metals with localized magnetic moments, *J. Appl. Phys.* **61**, 4393 (1987).
- [64] M. B. Fontes, J. C. Trochez, B. Giordanengo, S. L. Bud'ko, D. R. Sanchez, and E. M. Baggio-Saitovitch, Electron-magnon interaction in RNiBC (R=Er, Ho, Dy, Tb, and Gd) series of compounds based on magnetoresistance measurements, *Phys. Rev. B* **60**, 6781 (1999).
- [65] C. Butschkow, E. Reiger, A. Rudolph, S. Geissler, D. Neumaier, M. Soda, D. Schuh, G. Woltersdorf, W. Wegscheider, and D. Weiss, Origin of negative magnetoresistance of GaAs/(Ga,Mn)As core-shell nanowires *Phys. Rev. B* **87**, 245303 (2013).
- [66] P. W. Anderson, Localized Magnetic States in Metals, *Phys. Rev.* **124**, 41 (1961).
- [67] V. Vlasenko, K. Pervakov, S. Gavrilkin, Vortex pinning and magnetic phase diagram of $\text{EuRbFe}_4\text{As}_4$ iron-based superconductor, *Supercond. Sci. Technol.* **33**, 084009 (2020).
- [68] Yu. F. Eltsev, K. S. Pervakov, V. A. Vlasenko, S. Y. Gavrilkin, E. P. Khlybov, and V. M. Pudalov, Magnetic and transport properties of single crystals of Fe-based superconductors of the 122 family, *Phys.-Usp.* **57**, 827 (2014).

Appendix D: Supplemental Materials

Supplemental data to this article can be found online at It includes detailed information on the sample synthesis, XRD structural analysis, computational details of electron magnetotransport, electronic band structure (ARPES data and calculations).

1. SM I: Samples

The EuSn_2As_2 single crystals were synthesized from homogeneous SnAs (99.99% Sn + 99.9999% As) precursor and elemental Eu (99.95%) in stoichiometric molar ratio (2:1) using the growth method, similar to our previous works [7, 67, 68]. The initial high purity binary SnAs compound was obtained by the solid state reaction technique in quartz ampoule with residual argon atmosphere. Next, SnAs precursor and Eu were mixed with a 2:1 molar ratio; the mixture was placed in an alumina crucible and sealed in a quartz tube with residual argon pressure. The quartz tube was heated in a furnace up to 850 C° , held at this temperature for 12 h to homogenize melting, cooled down to 550 C° at a rate of $2^\circ/\text{h}$, and annealed at this temperature for 36 h. After that, the furnace was turned off, and the quartz tube was cooled down to room temperature inside the furnace. The synthesis protocol was used in our previous works [7, 67]; it is also similar to that described in Ref. [6]. The grown crystals had a shiny surface and could be easily exfoliated. More details on the flakes exfoliated from the buk crystals are given in Ref. [29].

2. SM II: XRD examination of the crystal structure.

In search for potential lattice defects that could cause scattering and NIMR we performed precise XRD examination of the bulk sample - its crystal structure and lattice defects evaluation.

Measurements were made with PanAlytical Ex'pert Pro X-ray diffractometer equipped with multiple crystal analyzers.

Figure 15 shows the presence of all possible peaks of the (00 l) series for a rhombohedral EuSn_2As_2 lattice ($l = 3n$, where n is an integer), as well as the absence of a noticeable broadening of the farthest reflections; these results are the evidence of a high structural perfection of the sample in the direction perpendicular to the basal plane.

Rocking curve (Fig. 16a) measured with the strongest reflection (00 15) demonstrates the absence of blocks in the bulk crystal, but indicates slight ($\sim 1^{-3}\text{rad}$) bending of the ab -plane towards one of the sample edges. Figure 16b measured with the 3rd analyzer crystal reveals a small spread in the lattice parameter for individual layers along the c axis. For the main maximum we

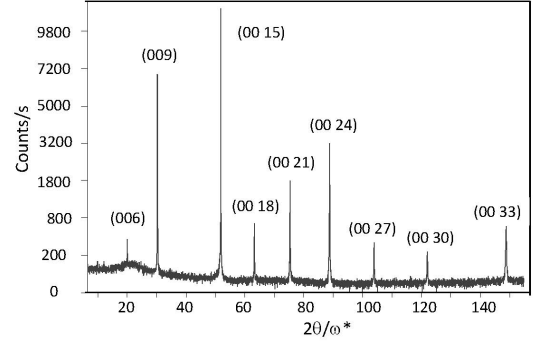


FIG. 15. X-ray diffraction pattern on a square scale for the studied EuSn_2As_2 bulk crystal from the side of the shiny surface. Correction for hybrid monochromator $\Delta(2\theta) = 0.0135^\circ$.

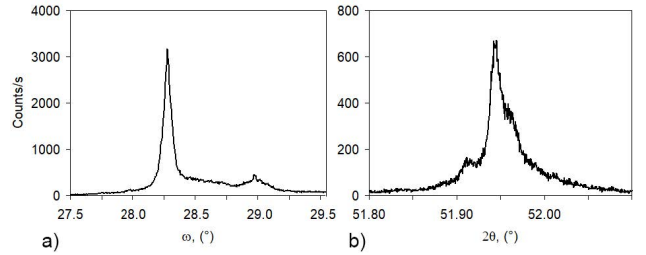


FIG. 16. (a) Rocking curve on the strongest reflection (00 15) with half-width $\Delta\omega = 0.067^\circ$. (b) $2\theta - \omega$ scanning curve measured with the third analyzer crystal.

find $2\theta = 51.9436^\circ$, and taking into account the correction for the hybrid monochromator, eventually, obtain $c = 26.3780\text{ \AA}$.

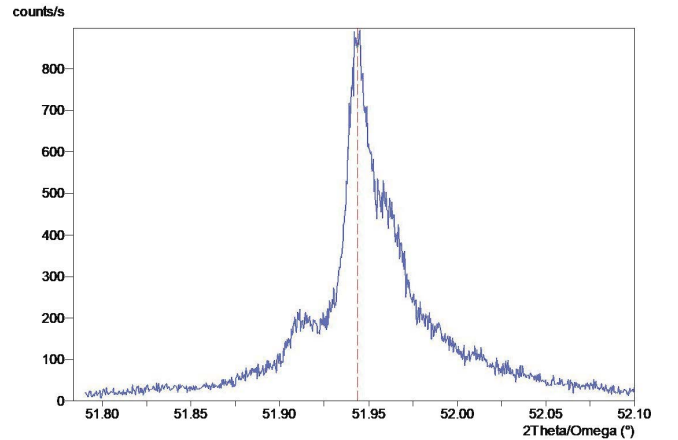


FIG. 17. $2\theta\omega$ scanning curve measured with the third analyzer crystal.

Figure 18a reveals a block structure, which is hidden in the symmetrical reflection. The lattice parameter in the basal plane was determined for the strongest peak. Note that all the curves without exception were measured under full illumination of the sample with X-ray beam.

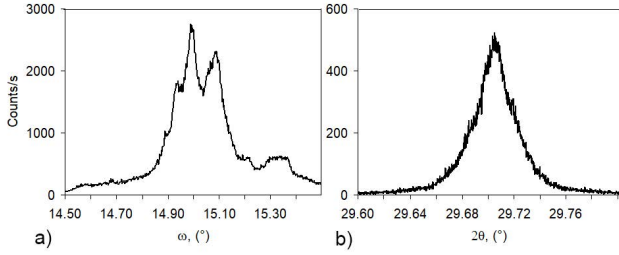


FIG. 18. (a) Rocking curve on asymmetric reflection (105) in the azimuthal position $\varphi = 12^\circ$. (b) The $(2\theta - \omega)$ -scanning curve with the third crystal-analyzer on the asymmetric reflection (105) in azimuthal position $\varphi = 12^\circ$.

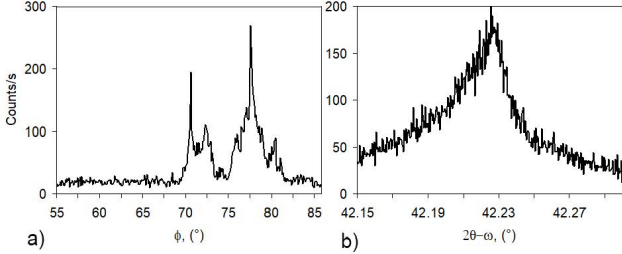


FIG. 19. (a) The ϕ -scanning curve about the normal to the basal plane on an asymmetric reflection (0110). (b) $(2\theta - \omega)$ -scanning curve with the third crystal-analyzer on asymmetric reflection (0110) in azimuthal position $\phi = 70.4^\circ$.

Based on the angular position of $2\theta_{(105)} = 29.7054^\circ$ in Fig. 18, taking into account the correction for the hybrid monochromator, and the known value $c = 26.3780\text{\AA}$, we find $a_{(105)} = 4.2190\text{\AA}$. Comparing with the literature data ($a = 4.2071\text{\AA}$, $c = 26.463\text{\AA}$), we conclude that in the studied crystal the lattice parameter along the c axis is lowered, and along the a axis is increased.

On the left panel of Fig. 19a, instead of one peak anticipated at $\phi = 72^\circ$ for the trigonal lattice, several peaks are seen, misoriented by $\Delta\phi = 7^\circ$. This means that the main defect in the crystal is twisting of weakly interconnected layers about the normal to the basal plane. From the angular position of the $2\theta_{(0110)} = 42.2254^\circ$ curve on the right panel of Fig. 19, and taking into account the correction for the hybrid monochromator and the known value $c = 26.3780\text{\AA}$, we find $a_{(0110)} = 4.2142\text{\AA}$. The asymmetry of the reflection is clearly seen, indicating the existence of layers with a large value of the lattice parameter in the basal plane.

a. Conclusion from the XRD examination

The studied crystal has one mirror shiny surface. Our XRD measurements evidence for the high quality of its crystal structure, both the diffractogram and the rocking curve testify the high structural perfection of the crystal. In more detail:

1. The lattice parameters of the studied crystal ($a_{(105)} = 4.2190\text{\AA}$, $c = 26.3780\text{\AA}$) are slightly larger in the basal plane and smaller in the perpendicular direction compared to the literature data ($a = 4.2071\text{\AA}$, $c = 26.463\text{\AA}$) [5, 10]. The 0.3% diminishing of the c -axis spacing might be related to the presence of 3% planar defects in which the Eu-Eu spacing is smaller by 0.16 nm (see section D 4 and [39]). However, the diminished defect layer thickness may cause only a factor of 10 smaller c -parameter squeezing (0.16nm/26.46nm, that is $0.7\% \times 3\% = 0.021\%$) insignificant to account for the measured 0.3% difference in the c -axis parameter with literature data.
2. The main defect of the studied crystal is the twisting (within $\approx 7^\circ$) of weakly coupled layers in the $a - b$ plane, perpendicular to the c -axis.

To summarize, no structural domains or blocks of different lattice orientations are found in the crystal. Thus, our XRD examination shows the absence of such macroscopic structural defects that can cause magnetic field dependent scattering of electrons. We note, however, that XRD is insensitive to purely magnetic defects.

3. SM III: Energy spectrum measurements and calculations

The aim of the energy spectrum measurements was (i) to verify that the studied samples have the same band structure as earlier studied [9], and (ii) to quantify the level splitting at the Fermi energy - the parameter required for the NIMR calculations. ARPES measurements were performed with UV He lamp source at 21.2eV photon energy. The samples were cleaved insitu in vacuum of 10^{-10} mBar. ARPES data were collected at sample temperature of 12K.

Figure 20 shows the energy spectrum in the wide range of energies. From these data we conclude that the band structure of the studied EuSn_2As_2 crystal is fully consistent with that in Ref. [9]. The spectrum measured in the narrow energy interval, in the vicinity of E_F , was shown in Fig. 3.

4. Planar nano-defects and weak ferromagnetism in the AFM ordered single crystal

From TEM measurements on a thin (30 nm) lamella cutout from the thick bulk crystal in the ac -plane we detected the presence of planar defects whose density is sample-dependent, and roughly amounts to $\sim 3\%$. These investigations are described in Ref. [39]. The planar defects have a local composition approximated as EuSnAs_2 . Such nanodefects are invisible by the conventional XRD technique. The DFT calculations [39] show that the planar defect has a local ferromagnetic moment. For the

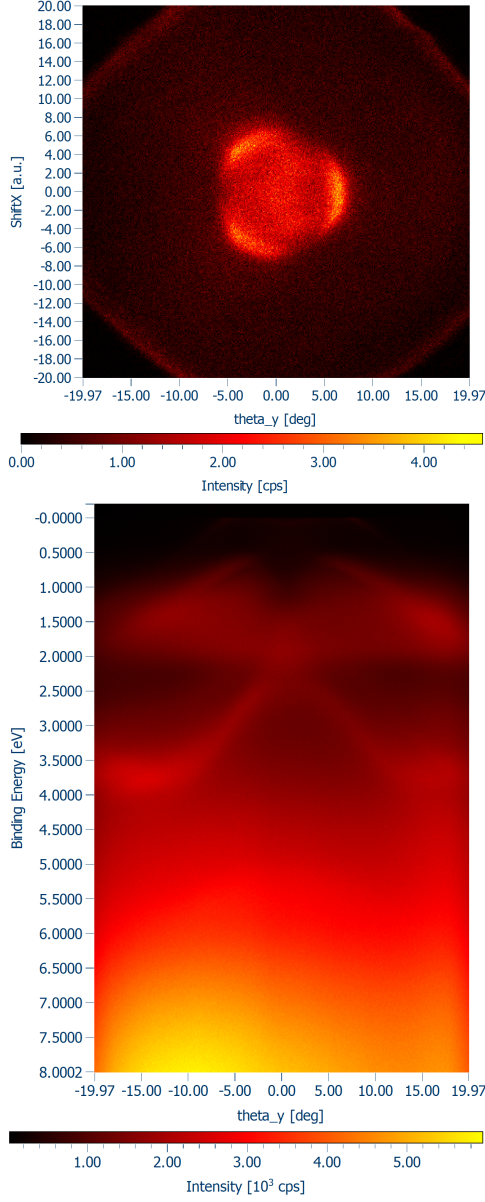


FIG. 20. (a) Fermi surface map along $k_y - k_x$ across $k_z = 0$ ($BE = 0$) at $\hbar\nu = 21.2$ eV and $T = 30$ K. (b) Electronic band dispersion along $M - \Gamma - M$; data are collected at $T = 12$ K with $\hbar\nu = 21.2$ eV.

purpose of the current paper it is important only that due to the small concentration of planar defects ($\sim 3 - 4\%$), and the small thickness (≈ 0.7 nm), much less than λ_F , they would rather unlikely to cause electron scattering and to affect the magnetotransport. However, their presence may induce a weak magnetization anisotropy in the easy ab -plane.